A distortion measure to validate and generate curved high-order meshes on CAD surfaces with independence of parameterization

A. Gargallo-Peiró[1], X. Roca[2*], J. Peraire[2] and J. Sarrate[1]

[1] *Laboratori de Càlcul Numèric (LaCàN), Departament de Matemàtica Aplicada III, Universitat Politècnica de Catalunya, Jordi Girona 1, E-08034 Barcelona, Spain.*
[2] *Department of Aeronautics and Astronautics, Massachusetts Institute of Technology, Cambridge, MA 02139, USA.*

SUMMARY

A framework to validate and generate curved nodal high-order meshes on CAD surfaces is presented. The proposed framework is of major interest to generate meshes suitable for thin-shell and 3D finite element analysis with unstructured high-order methods. First, we define a distortion (quality) measure for high-order meshes on parameterized surfaces that we prove to be independent of the surface parameterization. Second, we derive a smoothing and untangling procedure based on the minimization of a regularization of the proposed distortion measure. The minimization is performed in terms of the parametric coordinates of the nodes to enforce that the nodes slide on the surfaces. Moreover, the proposed algorithm repairs invalid curved meshes (untangling), deals with arbitrary polynomial degrees (high-order), and handles with low-quality CAD parameterizations (independence of parameterization). Third, we use the optimization procedure to generate curved nodal high-order surface meshes by means of an *a posteriori* approach. Given a linear mesh, we increase the polynomial degree of the elements, we curve them to match the geometry, and we optimize the location of the nodes to ensure mesh validity. Finally, we present several examples to demonstrate the features of the optimization procedure, and to illustrate the surface mesh generation process.

KEY WORDS: high-order methods; high-order mesh generation; quality measure; mesh optimization; curved elements; CAD ; parameterized surfaces

1. INTRODUCTION

In the last two decades, the solution of partial differential equations (PDEs) with unstructured high-order methods [1, 2, 3, 4, 5] has experimented a remarkable attention from the community of finite element methods (FEM). One of the main features that attracted this attention is the ability of unstructured high-order methods to converge exponentially with the order of the approximating polynomial when the exact solution of the PDE is smooth and without singularities [1, 6]. Accordingly, it has been possible to show that high-order methods provide higher accuracy with lower computational cost than low-order methods in a wide range of applications [7, 8, 9, 10, 11, 12, 13, 14, 15, 16].

*Correspondence to: Xevi Roca, Department of Aeronautics and Astronautics, Massachusetts Institute of Technology, Cambridge, MA 02139, USA. E-mail: xeviroca@mit.edu

Contract/grant sponsor: The first author was sponsored by CUR from DIUE of the *Generalitat de Catalunya* and the European Social Fund (grants FI-DGR'11 and BE-DGR'12), and by the Ferran Sunyer i Balaguer Foundation (grant FSB'13). The work of the corresponding author was partially supported by the Boeing Co. & US Air Force Office of Scientific Research & European Commission through the Boeing-MIT Alliance & the Computational Math Program & Marie Skłodowska-Curie Actions (HiPerMeGaFlowS individual fellowship grant).

To meet the theoretical convergence rate, and therefore enable the main advantages of unstructured high-order methods, it is required that the geometry is also approximated with high-order accuracy. To this end, in thin-shell finite element analysis the surface mesh has to be composed by curved elements represented by polynomials of the proper degree. Furthermore, these curved surface elements must have a non-singular (valid) and smooth (high-quality) normal vector to allow the computation of the weak formulation integrals on a master element. Analogously, in 3D finite element analysis the boundary faces (surface mesh) have to be also curved and fulfill the same validity and quality requirements. Note that in the 3D case the boundary faces must be valid (high-quality) to ensure also that the enclosed curved volume mesh is valid (high-quality). That is, if a boundary face of the mesh is folded (distorted), the corresponding volume element is also folded (distorted).

The advantages to approximate the domain surfaces with curved and smooth representations have been highlighted both for thin-shell [17, 18, 19, 20, 21, 22, 23, 24] and 3D [25, 26, 27, 28, 29, 20, 30] finite element analysis. It has been evidenced that using curved surface meshes mitigates the spurious errors that may arise from a piece-wise linear approximation of the domain surfaces, especially when a high-order approximation of the solution of a PDE is required. Accordingly, the generation of valid and high-quality curved surface meshes is considered mandatory to exploit all the advantages of unstructured high-order methods.

The direct generation of curved surface meshes is not only required in thin-shell finite element analysis with unstructured high-order methods. It is also a crucial step of the standard *a posteriori* approach used to generate high-order volume meshes suitable for 3D analysis [27, 31, 32, 33, 34, 35, 36, 37, 38, 39]. The goal of this approach is to indirectly generate a high-order volume mesh that matches a curved boundary. First, a valid initial linear mesh is generated with any established unstructured mesh generator. Second, the volume mesh is converted to high-order and its boundary faces are curved to match properly the initial geometry. In this step, invalid elements can be generated since the newly curved faces can intersect with the internal faces of the volume elements. Hence, it is necessary a final step where the position of the mesh nodes is optimized or the topology be modified to obtain a valid and high-quality mesh. The final step of the *a posteriori* approach, where the volume elements are curved and repaired, has received an increasing attention in the last fifteen years. Surprisingly, the generation of valid curved surface meshes, the second step of the *a posteriori* approach, has received less attention besides of its major importance both in thin-shell and 3D finite element analysis.

The most challenging difference between the generation of curved volume meshes and curved surface meshes is that whereas interior volume nodes can move freely inside the container volumes, surface nodes can only slide on the surface where they lie. Specifically, it is required to involve the representation of the domain surfaces as a constraint in the optimization procedure. To this end, we assume that a CAD model represents the boundary surfaces since it provides some advantages when compared with other standard surface representations. First, CAD surface representations are more accurate than the piece-wise linear approximations determined by triangular meshes. Second, they provide explicit parameterizations of the surfaces as opposed to implicit surface representations. Finally, CAD models are generated in the standard design process and therefore, they are well suited for industrial applications of unstructured high-order methods.

The aim of this work is to generate valid and high-quality high-order meshes on parameterized CAD surfaces by means of an *a posteriori* procedure. To achieve this goal we present three main contributions. First, we define a distortion (quality) measure for nodal high-order meshes with the nodes on parameterized surfaces. The proposed measure quantifies the deviation between an ideal and a physical surface mesh, and it is expressed in terms of the parametric coordinates of the mesh nodes. Moreover, we prove that this definition is independent of the selected surface parameterization.

Second, we derive a smoothing and untangling procedure to optimize the quality of high-order meshes of any polynomial degree (high-order) on CAD surfaces. The proposed optimization approach is developed on the parametric space of the surface, ensuring that the nodes always lie on the exact CAD geometry. Moreover, it is capable to transform an invalid curved high-order mesh to

a valid mesh (untangling). In addition, we prove that the optimization procedure is also independent of the parameterization. Hence, we obtain a method that generates untangled (valid) and smoothed (high-quality) curved high-order meshes from the exact CAD representation regardless of the quality of its parameterization.

Finally, we propose an *a posteriori* curved surface mesh generation approach based on the proposed optimization technique. The approach consists on modifying an initial surface linear mesh of a CAD geometry by: first, introducing high-order nodes on the parametric space; second, curving the surface mesh by mapping the parametric high-order nodes through the surface parameterization; and third, using the optimization procedure to obtain a final parametric configuration that, once mapped to the physical CAD surface, generates a valid and high-quality surface mesh. The resulting curved high-order surface meshes can be used either to perform thin-shell analysis or to determine the curved boundary surface meshes in a volume mesh curving method. Specifically, we use this method to provide valid boundary conditions, *i.e.* curved surface meshes, in our curved high-order tetrahedral mesh generator [39].

The rest of the paper is organized as follows. First, in Sec. 2 we review the related work on surface mesh optimization and generation of high-order meshes. Next, in Sec. 3 we present the scope of this work, the statement of the problem that we aim to solve, and the selected approach. In Sec. 4, we set the framework for the definition of point-wise distortion measures for high-order elements on parameterized surfaces. In Sec. 5, we detail an smoothing and untangling procedure based on the minimization of the proposed distortion measures. Following, in Sec. 6 we use the point-wise measures to define a distortion (quality) measure for high-order elements on parameterized CAD surfaces. Finally, we present several examples to underline the main properties of the proposed optimization method and the derived mesh generation procedure, Sec. 7.

2. RELATED WORK

A crucial step in the *a posteriori* process is to detect invalid elements. For planar and volumetric high-order elements several approaches have been proposed to detect the validity of the representation mapping [40, 27, 31, 32, 33, 34, 41, 42, 43], and to define suitable quality measures [44, 45, 46, 47, 48, 49, 50, 51, 52, 53]. However, these works do not the define quality measures for curved high-order meshes on parameterized surfaces. On the contrary, we present a new technique to extend the Jacobian-based distortion measures for planar linear triangles presented in [54, 55], to curved nodal high-order elements of any polynomial degree on parameterized surfaces. Specifically, we define the distortion (quality) measure as the deviation of the physical high-order element with respect to an ideal triangle, as it is proposed in [51, 53] for planar and volumetric curved high-order elements. Similarly to our previous work for linear elements [56], we express the developed measure in terms of the parametric coordinates of the mesh nodes and we prove that it is independent of the surface parameterization.

A posteriori methods to generate high-order surface meshes can be classified into three groups according to the technique used to curve the mesh and match the domain boundary. The first group of methods [57, 33, 58, 59, 60] curve the surface mesh boundary and apply local topological operations, such as refinement, edge removal, or edge and face swapping, to adapt the mesh topology to the curved surfaces. Then, edge nodes and inner face nodes are relocated. For instance, reference [57] deals with quadratic elements, and proposes to relocate the mid-edge nodes to enforce that the tangent vectors at the vertices of the boundary tetrahedral faces verify a geometrical criterion. Later, references [33, 58] extended to higher polynomial degrees the topology modification techniques, and proposed a method to curve the inner edges of the surface mesh according to their distance to the geometry curves. A similar approach based on topological operations and node relocation is also used in references [59, 60]. The goal of these works is to generate a curved high-order surface mesh when the exact CAD representation is not available and the geometry is approximated by a triangulation.

The second group of methods curves the initial linear mesh using an elasticity analogy. For instance, in reference [35] the surface parameterization is used to write the elasticity problem in

terms of the parametric coordinates of the surface nodes, leading to a non-linear minimization problem.

The third group of methods presents two alternatives to generate surface meshes by means of optimization procedures. On the one hand, reference [37] formulates a local optimization approach that uses the surface geodesics to compute the location of the surface nodes. The proposed algorithm requires an additional projection step to ensure that the inner face nodes lie on the exact physical surface. On the other hand, references [61, 38] propose a global optimization method for high-order tetrahedral meshes that constrains the displacements of the surface nodes using the surface parameterization. In order to avoid tangled elements a log-barrier approach [62] is used to penalize small values of the determinant of the Jacobian. Our approach belongs to this third group. We propose a global non-linear least-squares optimization based on the minimization of a distortion measure. However, to untangle invalid configurations we regularize the distortion measure according to [63, 56].

3. PROBLEM STATEMENT AND METHODOLOGY

3.1. Input and output

Our input data is a linear mesh $\mathcal{M}^1_{\mathbf{x}}$ composed by elements with the nodes on a parameterized surface. We assume that the input linear mesh is valid and that it has elements of the desired shape and size. We also assume that the surface Σ is parameterized by a continuously differentiable and invertible mapping (diffeomorphism)

$$\begin{array}{rccc} \boldsymbol{\varphi}: & \mathcal{V} \subset \mathbb{R}^2 & \longrightarrow & \Sigma \subset \mathbb{R}^3 \\ & \mathbf{u} = (u, v) & \longmapsto & \mathbf{x} = \boldsymbol{\varphi}(\mathbf{u}), \end{array} \tag{1}$$

where $\mathcal{V}$ is the parametric space of the surface. In this work, we use the OpenCASCADE library [64] to retrieve the parameterization of the surfaces of a CAD model.

The output data is a high-order mesh $\mathcal{M}^p_{\mathbf{x}}$ of polynomial degree p with all the nodes on the parameterized surface, and composed by valid elements (non-null and positively oriented normal of the representation mapping) that have a shape close to the initial straight-sided linear elements.

3.2. Methodology

The proposed approach is composed by the following four steps.

1. *Generate a linear mesh on the parameterized surface.*
   Using any established linear surface mesh generator we create a mesh with elements of the desired size and shape. Our approach requires to know both the physical, $\mathcal{M}^1_{\mathbf{x}}$, and the parametric, $\mathcal{M}^1_{\mathbf{u}}$, coordinates of the nodes of the initial linear surface mesh. There are two strategies to retrieve the parametric coordinates of the nodes. On the one hand, we can require that the linear mesh generator stores the parametric coordinates, see [65, 66]. On the other hand, we can solve a non-linear problem to obtain the parametric coordinates of the closest point on the surface to each of the mesh nodes, see [67]. In Figure 1(a) we show the linear mesh generated on a propeller. We have colored the mesh elements according to their shape quality taking as ideal element the equilateral triangle.

2. *Set the ideal mesh.*
   We increase the polynomial degree of the mesh on the physical space and we set this straight-sided high-order mesh as the ideal configuration in our optimization procedure. Note that this mesh is of the desired polynomial degree and, at the same time, has elements of the desired size and shape. It is important to highlight that the coordinates of the ideal mesh nodes will be fixed during the optimization procedure.

3. *Set the initial curved high-order mesh and a valid curved mesh boundary.*
   We define a distribution of nodes of degree p on the straight-sided elements on the parametric

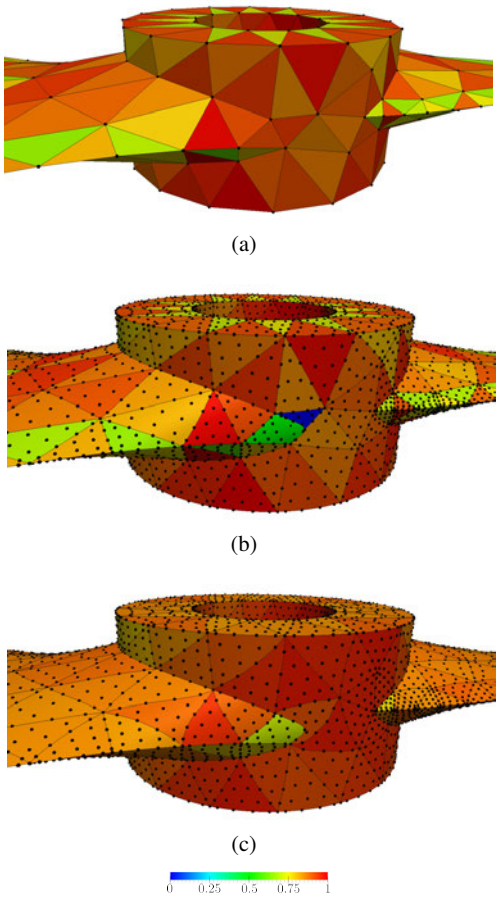

Figure 1. Process of the generation of a high-order mesh on a propeller: (a) linear mesh, (b) initial (invalid) curved mesh of polynomial degree five, and (c) optimized (valid) mesh of polynomial degree five.

space. For elements adjacent to the surface boundary, we blend the boundary edges to match the corresponding geometry curve. Next, we define a Legendre-Gauss-Lobatto distribution of the nodes [68] along the edge using the arc parameter of the curve. Then, the inner nodes of the elements are redistributed by means of the blending presented in [68]. We denote the mesh with the nodes on the parametric space as the initial parametric mesh, $\mathcal{M}_{\mathbf{u}}^{p,0}$. Afterwards, we map $\mathcal{M}_{\mathbf{u}}^{p,0}$ to the surface, obtaining an initial high-order physical mesh, $\mathcal{M}_{\mathbf{x}}^{p,0}$, see details in [65, 66].

The high-order meshes obtained after these steps can contain tangled elements. For instance, Figure 1(b) shows a detail of the mesh of interpolation degree five for the propeller with a tangled element colored in blue. These inverted elements appear due to two main issues. First, the *a posteriori* curving of the boundary edges to match the geometry curves can lead to intersections between two element edges, see Figure 2(a). Second, a valid high-order distribution on the parametric space can be invalid once mapped onto the surface due to a low-quality parameterization, see Figure 2(b).

4. *Obtain a valid curved configuration of the high-order mesh.*
We optimize (smooth and untangle) the location of all the nodes that are not on the boundary of the domain. Specifically, we modify their location in the parametric space to repair the existent inversions and to improve the quality of the high-order elements on the surface. In this manner, we obtain a mesh $\mathcal{M}_{\mathbf{u}}^{p}$ on the parametric space that leads to a high-quality mesh on the physical surface. Next, by means of the surface parameterization $\boldsymbol{\varphi}$, we map the

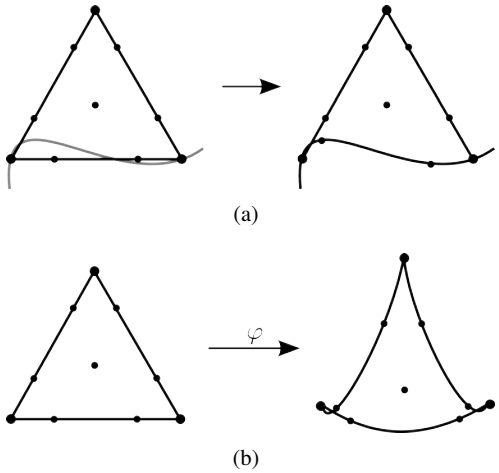

Figure 2. Possible tangling issues in the curving procedure: (a) element edge curving to fit the boundary geometry that creates an auto-intersection with an inner edge, and (b) anisometric parameterization that produces an invalid element on the physical space.

parametric mesh to the surface, $\mathcal{M}^p_{\mathbf{x}} = \boldsymbol{\varphi}(\mathcal{M}^p_{\mathbf{u}})$. Comparing the initial linear mesh, Figure 1(a), and the final mesh, Figure 1(c), we realize that we have been able to obtain a valid and high-quality high-order mesh such that the shape of its elements resembles the shape of the elements in the initial linear mesh.

We point out that this work is devoted to the fourth step of the presented process. Specifically, we define a distortion measure to determine the validity of a high-order element with the nodes on a parameterized surface, see Sec. 4.3, and we derive an optimization (smoothing and untangling) process in terms of the parametric coordinates of the nodes to improve the quality of the initial mesh, see Sec. 5.3. Note that we are focused on the generation of nodal high-order triangular elements of degree p. Nevertheless, changing the element shape functions in Sec. A, the same approach is applicable to high-order quadrilateral surface meshes.

4. POINT-WISE DISTORTION MEASURES FOR SURFACES

In this section, we present a technique to define a point-wise measure of the distortion of a mapping between surfaces in $\mathbb{R}^3$. To this end, we first review the standard distortion measures for linear elements, Sec. 4.1. Next, in Sec. 4.2, we propose a technique to extend this measures to quantify the distortion of mappings between pairs of vectors in $\mathbb{R}^3$. Finally, in Sec. 4.3, we use the measures presented in Sec. 4.2 to define a point-wise distortion measure for mappings between surfaces.

4.1. Distortion measures for linear elements

In this work, we use the Jacobian-based distortion measures framework for linear elements presented in [54, 55]. In order to define the distortion of a linear triangle in the physical space, E^P, we consider the ideal triangle, E^I, that represents the desired geometrical properties (shape, size, stretching...). To measure the deviation between these two elements, we consider the unique affine mapping, $\boldsymbol{\phi}_E$, from E^I to E^P, see Fig. 3. To compute $\boldsymbol{\phi}_E$, we consider the master element, E^M, and we introduce two additional affine mappings: $\boldsymbol{\phi}_P$, between the master and the physical elements, and $\boldsymbol{\phi}_I$, between the master and the ideal elements. Thus, $\boldsymbol{\phi}_E$ is determined by the composition

$$\boldsymbol{\phi}_E : E^I \xrightarrow{\boldsymbol{\phi}_I^{-1}} E^M \xrightarrow{\boldsymbol{\phi}_P} E^P.$$

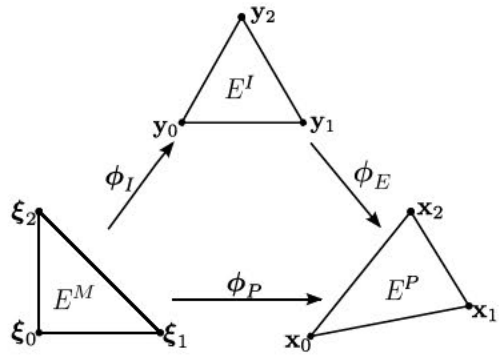

Figure 3. Mappings between the master, ideal and physical linear elements.

Since ϕ_E is affine, its Jacobian, $\mathrm{D}\phi_E \in \mathbb{R}^2 \times \mathbb{R}^2$, is constant inside the element. Note that the Jacobian of ϕ_E encodes the deviation of the translation-invariant features of the physical element with respect to the ideal one. Hence, several distortion measures of the physical element can be defined in terms of $\mathrm{D}\phi_E$. These distortion measures, herein denoted by η, quantify the deviation of one or several features (shape, size, skewness, degeneracy,...) of the physical element with respect to the ideal one in the scale range $[1, \infty)$. These measures assign $\eta = 1$ to the ideal element, and tend to infinity as the element features degenerate. The corresponding quality measure is defined as

$$q := \frac{1}{\eta} \in [0, 1]. \tag{2}$$

For the remaining of this work, we use the shape distortion measure [54]:

$$\eta(\mathrm{D}\phi_E) \quad = \quad \frac{\|\mathrm{D}\phi_E\|^2}{2\,|\sigma|}, \tag{3}$$

where $\|\cdot\|$ is the Frobenius norm, and $\sigma = \det(\mathrm{D}\phi_E)$. This distortion measure quantifies the deviation of the shape of the physical triangle with respect to the shape of the ideal triangle.

To untangle meshes in the optimization procedure, we use the regularization of the determinant σ proposed in [63]. This regularization can be applied to Jacobian-based distortion measures where the determinant of the Jacobian appears in the denominator. Specifically, we replace σ in Eq. (3) by

$$\sigma_\delta(\sigma) = \frac{1}{2}\left(\sigma + \sqrt{\sigma^2 + 4\delta^2}\right), \tag{4}$$

where δ is an element-wise constant parameter that is determined automatically according to the size of the corresponding ideal element, see details in [39, 69]. Therefore, we consider the regularized distortion measure,

$$\eta_\delta(\mathrm{D}\phi_E) = \frac{\|\mathrm{D}\phi_E\|^2}{2\,|\sigma_\delta|}. \tag{5}$$

It is important to point out that without the proposed regularization, η has an asymptote when $\sigma = 0$ (where an element becomes non-valid). Note that it is required to regularize σ to remove this asymptote and therefore, allow to the optimization procedure recovering from the non-valid configuration (tangled). For $\delta > 0$, $\sigma_\delta(\sigma)$ is a strictly increasing function, such that $\sigma_\delta(0) = \delta$ and that tends to 0 when σ tends to $-\infty$. Therefore, η_δ is a smooth function with no asymptotes. Moreover, for small values of δ, the minimum of η_δ is close to the valid minimum of η_0.

4.2. Distortion measure for linear mappings between planes in 3D

The distortion measures for linear elements, see Eq. (5), are defined in the terms of a 2×2 matrix that corresponds to a linear mapping J between pairs of vectors in $\mathbb{R}^2$. However, linear surface

meshes lead to planar elements immersed in $\mathbb{R}^3$ and therefore, distortion measures have to be defined in terms of a linear mapping between pairs of vectors in $\mathbb{R}^3$. Hence, the expression of the distortion measure for linear planar elements cannot be applied directly. To address this issue, in this section we determine a 2×2 matrix $\bar{\mathbf{J}}$ in planar cartesian coordinates that features the same distortion of $\mathbf{J}$.

Let $\Pi_a, \Pi_b \subset \mathbb{R}^3$ be two planes on $\mathbb{R}^3$, determined by two pairs of vectors $\mathbf{a}_1, \mathbf{a}_2 \in \Pi_a$ and $\mathbf{b}_1, \mathbf{b}_2 \in \Pi_b$, respectively. Let $\mathbf{J} : \Pi_a \subset \mathbb{R}^3 \to \Pi_b \subset \mathbb{R}^3$ be a linear mapping such that

$$\mathbf{b}_i = \mathbf{J}(\mathbf{a}_i), \qquad i = 1, 2.$$

First, we obtain an orthonormal basis for Π_a by means of the Gram-Schmidt procedure. Specifically, we define

$$\begin{aligned} \tilde{\mathbf{a}}_1 &:= \frac{\mathbf{a}_1}{\|\mathbf{a}_1\|}, \\ \tilde{\mathbf{a}}_2 &:= \gamma \frac{\mathbf{a}_2 - (\mathbf{a}_2^T \tilde{\mathbf{a}}_1)\, \tilde{\mathbf{a}}_1}{\|\mathbf{a}_2 - (\mathbf{a}_2^T \tilde{\mathbf{a}}_1)\, \tilde{\mathbf{a}}_1\|}, \end{aligned}$$

as the two orthonormal vectors of the new basis, where γ is defined to ensure a well oriented orthonormal basis. In particular, we set γ equal to 1 or -1 for counter-clockwise or clockwise oriented vectors, respectively.

Note that the 2×3 matrix $\tilde{\mathbf{A}}^T$, where $\tilde{\mathbf{A}} = [\tilde{\mathbf{a}}_1 \ \tilde{\mathbf{a}}_2]$, expresses $\mathbf{a}_i$ in the orthonormal basis $\tilde{\mathbf{a}}_i$. Analogously, we denote by $\tilde{\mathbf{b}}_1$ and $\tilde{\mathbf{b}}_2$ the two vectors of the orthonormal basis of Π_b, and $\tilde{\mathbf{B}} := [\tilde{\mathbf{b}}_1 \ \tilde{\mathbf{b}}_2]$. Therefore, $\tilde{\mathbf{B}}^T$ expresses $\mathbf{b}_i$ in the orthonormal basis $\tilde{\mathbf{b}}_i$.

Finally, we define the vectors

$$\bar{\mathbf{a}}_i := \tilde{\mathbf{A}}^T \mathbf{a}_i, \qquad i = 1, 2 \tag{6}$$

and

$$\bar{\mathbf{b}}_i := \tilde{\mathbf{B}}^T \mathbf{b}_i, \qquad i = 1, 2 \tag{7}$$

to determine in planar cartesian coordinates a linear mapping $\bar{\mathbf{J}}$ such that

$$\bar{\mathbf{b}}_i = \bar{\mathbf{J}} \bar{\mathbf{a}}_i, \qquad i = 1, 2. \tag{8}$$

Note that $\bar{\mathbf{J}}$ has the same distortion measure value as $\mathbf{J}$, since η_δ, see Equation (5), is invariant under rotation. To obtain the expression of the matrix $\bar{\mathbf{J}}$, we substitute Equations (6) and (7) in Equation (8):

$$\tilde{\mathbf{B}}^T \mathbf{b}_i = \bar{\mathbf{J}}\ \tilde{\mathbf{A}}^T \mathbf{a}_i.$$

In particular, defining $\mathbf{A} := [\mathbf{a}_1 \ \mathbf{a}_2]$, and $\mathbf{B} := [\mathbf{b}_1 \ \mathbf{b}_2]$, we have that

$$\tilde{\mathbf{B}}^T \mathbf{B} = \bar{\mathbf{J}}\ \tilde{\mathbf{A}}^T \mathbf{A}.$$

Since $\mathbf{a}_1$ and $\mathbf{a}_2$ determine a plane Π_a, they are linearly independent. Thus, they determine two linearly independent vectors $\tilde{\mathbf{a}}_1$ and $\tilde{\mathbf{a}}_2$. Consequently, $\tilde{\mathbf{A}}^T \mathbf{A}$ is a 2×2 invertible matrix and therefore, we have that matrix $\bar{\mathbf{J}}$ can be computed from $\mathbf{A}$ and $\mathbf{B}$ as

$$\bar{\mathbf{J}}(\mathbf{A}, \mathbf{B}) := \tilde{\mathbf{B}}^T \mathbf{B}\ (\tilde{\mathbf{A}}^T \mathbf{A})^{-1}, \qquad i = 1, 2. \tag{9}$$

Finally, we can define the distortion of the linear map $\mathbf{J}$ in terms of the matrix $\bar{\mathbf{J}}$ and of the regularized distortion measure η_δ for linear elements as $\eta_\delta(\bar{\mathbf{J}})$.

4.3. Point-wise distortion measure for mappings between surfaces

In this section, we define a measure of the distortion of a mapping between two surfaces. We assume that we have an ideal surface $\Sigma_I \subset \mathbb{R}^3$ and a physical surface $\Sigma_P \subset \mathbb{R}^3$, that are diffeomorphic to the same planar domain $\Sigma_R \subset \mathbb{R}^2$. In particular, Σ_I and Σ_P are also diffeomorphic and therefore,

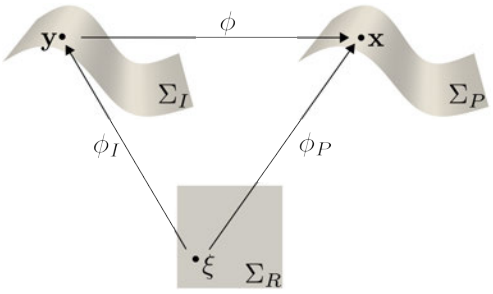

Figure 4. Mappings between the physical, ideal and reference surfaces.

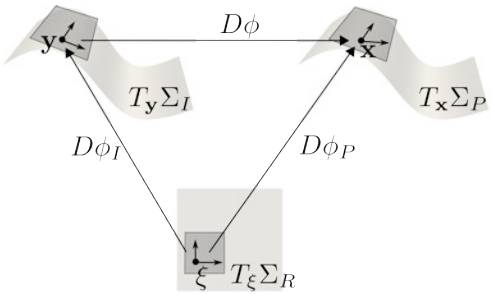

Figure 5. Mappings between the tangent spaces of the surfaces.

the physical surface can be defined as the image of a diffeomorphism ϕ from Σ_I to Σ_P, see Fig. 4. To define the distortion measure $\mathrm{M}\phi$ for mappings ϕ between surfaces, we will pose M in terms of a given distortion measure for linear elements η_δ.

We consider two diffeomorphisms between the reference surface, and the physical and ideal surfaces:

$$\phi_I : \Sigma_R \subset \mathbb{R}^2 \longrightarrow \Sigma_I \subset \mathbb{R}^3,$$
$$\phi_P : \Sigma_R \subset \mathbb{R}^2 \longrightarrow \Sigma_P \subset \mathbb{R}^3.$$

Then, the diffeomorphism ϕ between the ideal and physical surfaces can be expressed as $\phi = \phi_P \circ \phi_I^{-1}$. In particular, ϕ is a mapping which Jacobian $\mathbf{J}(\mathbf{y}) := \mathbf{D}\phi(\mathbf{y})$ defines a linear mapping between the tangent space at a point $\mathbf{y}$ in Σ_I, and the tangent space at a point $\mathbf{x} = \phi(\mathbf{y})$ in Σ_P, see Figure 5. Next, using the applications

$$\mathbf{D}\phi_I : \mathrm{T}_{\boldsymbol{\xi}}\Sigma_R \longrightarrow \mathrm{T}_{\mathbf{y}}\Sigma_I,$$
$$\mathbf{D}\phi_P : \mathrm{T}_{\boldsymbol{\xi}}\Sigma_R \longrightarrow \mathrm{T}_{\mathbf{x}}\Sigma_P,$$

we compute the expression of $\mathbf{J}$ on cartesian coordinates, $\bar{\mathbf{J}}(\mathbf{D}\phi_I, \mathbf{D}\phi_P)$, presented in Eq. (9).

In this manner, we can define the point-wise distortion for the mapping ϕ at a point $\mathbf{y}$ on Σ_I as:

$$\mathrm{M}\phi := \eta_\delta(\bar{\mathbf{J}}(\mathbf{D}\phi_I, \mathbf{D}\phi_P)). \tag{10}$$

Note that the distortion M for the mapping ϕ is casted to evaluate a distortion measure η_δ for linear mappings, see Eq. (5). Therefore, it is well defined since $\bar{\mathbf{J}}(\mathbf{D}\phi_I, \mathbf{D}\phi_P)$ defines a linear mapping for any $\mathbf{y}$ on Σ_I.

5. GENERATION OF NODAL HIGH-ORDER MESHES ON PARAMETERIZED SURFACES

In this section, we formulate an optimization problem to generate a valid curved high-order mesh by means of an *a posteriori* approach. First, we characterize the best diffeomorphism

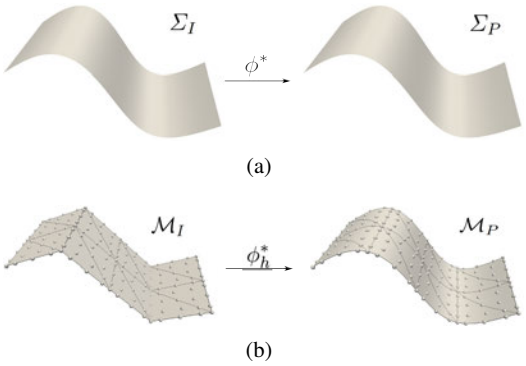

Figure 6. (a) Mapping between the ideal and physical surfaces. (b) Mapping between the ideal and physical meshes.

between two surfaces, Sec. 5.1. Next, we discretize the continuous characterization for the desired diffeomorphism, Sec. 5.2. Since our objective is to generate nodal high-order meshes on parameterized surfaces, in Section 5.3 we present the resulting optimization problem posed in terms of the parametric coordinates of the mesh nodes. Finally, in Sec. 5.4, we prove that the proposed distortion measure and the obtained objective function are independent of the surface parameterization.

5.1. Curving: globally defined smooth mapping

Fixed an ideal surface Σ_I and the boundary of the physical surface, $\partial\Sigma_P$, our goal is to find the best mapping, ϕ^* in $\mathcal{C}^1(\Sigma_I, \Sigma_P)$, between both surfaces according to the distortion measure M, see Eq. (10). Specifically, the ideal mapping ϕ^*, see Figure 6(a), would be a local diffeomorphism such that

$$\mathrm{M}\phi^* = 1, \quad \text{in } \Sigma_I, \tag{11}$$
$$\phi^* = g, \quad \text{on } \partial\Sigma_I, \tag{12}$$

where the boundary $\partial\Sigma_P$ is known and determined by the mapping g from $\partial\Sigma_I$ to $\partial\Sigma_P$.

5.2. Curving: element-wise defined smooth mapping

Our goal is to a curve a straight-sided ideal mesh $\mathcal{M}_I$, that approximates the surface Σ_I, to obtain a curved high-order mesh $\mathcal{M}_P$ that matches the surface Σ_I. To this end, we seek a mapping ϕ_h^*, see Fig. 6(b), such that it is an element-wise local diffeomorphism for all E^I in $\mathcal{M}_I$ and it has an ideal distortion measure $\mathrm{M}\phi_h^*$. This ideal mapping ϕ_h^* can be characterized as the element-wise polynomial diffeomorphism such that

$$\mathrm{M}\phi_h^* = 1, \quad \text{in } \mathcal{M}_I, \tag{13}$$
$$\phi_h^* = g_h, \quad \text{on } \partial\mathcal{M}_I, \tag{14}$$

where the curved boundary mesh $\partial\mathcal{M}_P$ is known and determined by the mapping g_h from $\partial\mathcal{M}_I$ to $\partial\mathcal{M}_P$.

To ensure that the obtained curved mesh matches the physical surface, we consider a mesh representation that constrains the element nodes to be on the parameterized surface. Specifically, for a mesh $\mathcal{M}_I$ composed by the union of n_E ideal elements E_e^I, $e = 1, \cdots, n_E$, we enforce that ϕ_h^* is in the set of continuous vector functions in the ideal mesh

$$\begin{aligned} \boldsymbol{\mathcal{W}} := \big\{ \mathbf{w} \in \left[\mathcal{C}^0\left(\mathcal{M}\right)\right]^3 \mid \\ \mathbf{w}_{|_{E^I}} \in \boldsymbol{\mathcal{W}}_{\boldsymbol{E^I}},\ \forall E^I \in \mathcal{M}_I \big\}, \end{aligned} \tag{15}$$

where

$$\boldsymbol{\mathcal{W}}_{\boldsymbol{E}^I} := \left\{ \mathbf{w} \in \left[\mathcal{P}^p(E^I)\right]^3 \;\middle|\; \mathbf{w} = \sum_{i=1}^{n_p} \boldsymbol{\varphi}(\mathbf{u}_i) N_i(\mathbf{y}) \quad \text{for } \mathbf{u}_1, \ldots, \mathbf{u}_{n_p} \in \mathcal{V} \right\} \tag{16}$$

is a set functions in the ideal element, and $\mathcal{P}^p(E^I)$ is the space of polynomials of degree p on the element E^I, $\{N_i\}_{i=1,\ldots,n_p}$ are polynomial interpolative shape functions of degree p, and n_p is the number of element nodes. Hence, the physical nodes of an element, $\mathbf{x}_i$ in Σ_P, can be expressed in terms of their parametric coordinates as $\mathbf{x}_i = \boldsymbol{\varphi}(\mathbf{u}_i)$, where $\mathbf{u}_i$ in $\mathcal{V}$, and $\boldsymbol{\varphi}$ is the surface parameterization in Eq. (1), see details in Appendix A. In this manner, if we modify the parametric coordinates of a node $\mathbf{u}_i$, its physical location will always be on the surface.

Note that fixed $\mathcal{M}_I$ and determined $\partial\mathcal{M}_P$ in Eq. (14), a mapping ϕ_h^* such that Eq. (13) is verified may be, in general, not achievable. Therefore, this condition is imposed in a least-squares sense. That is, we seek ϕ_h^* in $\boldsymbol{\mathcal{W}_D}$ such that

$$\phi_h^* \;=\; \underset{\phi_h \in \boldsymbol{\mathcal{W}_D}}{\operatorname{argmin}} \|\mathrm{M}\phi_h - 1\|^2_{\mathcal{M}_I}, \tag{17}$$

where

$$\boldsymbol{\mathcal{W}_D} := \{\phi_h \in \boldsymbol{\mathcal{W}} \;|\; (\mathrm{M}\phi_h - 1) \in \mathcal{L}^2(\mathcal{M}_I), \text{ and } \phi_h = g_h \text{ on } \partial\mathcal{M}_I\}.$$

In Eq. (17), we define the norms

$$\|f\|_{\mathcal{M}_I} \;:=\; \sqrt{\langle f, f\rangle_{\mathcal{M}_I}}, \tag{18}$$

$$\|f\|_{E^I} \;:=\; \sqrt{\langle f, f\rangle_{E^I}}, \tag{19}$$

in terms of the inner product of two scalar functions on $\mathcal{M}_I$ as

$$\langle f, g\rangle_{\mathcal{M}_I} \;:=\; \sum_{e=1}^{n_E} \langle f_{|_{E_e^I}}, g_{|_{E_e^I}}\rangle_{E_e^I}, \tag{20}$$

$$\langle f, g\rangle_{E^I} \;:=\; \int_{E^I} f(\mathbf{y})\, g(\mathbf{y})\, \mathrm{d}\mathbf{y}. \tag{21}$$

Once ϕ_h^* is determined, we define the mesh $\mathcal{M}_P$ of the physical surface Σ_P as the image of $\mathcal{M}_I$ by ϕ_h^*. To this end, each physical element is obtained as:

$$E_e^P = \phi_h^*(E_e^I) \tag{22}$$

and then the physical mesh is obtained as the union of the elements E_e^P, for $e = 1, \cdots, n_E$.

5.3. Curving: nodal high-order mesh optimization on parametric coordinates

The minimization problem stated in Eq. (17) can be rewritten in terms of elemental contributions. In particular, according to Eq. (18) and (20) we seek ϕ_h^* in $\boldsymbol{\mathcal{W}_D}$ such that :

$$\begin{aligned} \phi_h^* &= \underset{\phi_h \in \boldsymbol{\mathcal{W}_D}}{\operatorname{argmin}} \|\mathrm{M}\phi_h - 1\|^2_{\mathcal{M}_I} \\ &= \underset{\phi_h \in \boldsymbol{\mathcal{W}_D}}{\operatorname{argmin}} \sum_{e=1}^{n_E} \|\mathrm{M}\boldsymbol{\phi}_{h_{|_{E_e^I}}} - 1\|^2_{E_e^I} \\ &= \underset{\phi_h \in \boldsymbol{\mathcal{W}_D}}{\operatorname{argmin}} \sum_{e=1}^{n_E} \|\mathrm{M}\boldsymbol{\phi}_{E_e} - 1\|^2_{E_e^I}. \end{aligned} \tag{23}$$

where $\boldsymbol{\phi}_{E_e} := \boldsymbol{\phi}_{h|_{E_e^I}}$ is the mapping between the ideal E_e^I and physical element E_e^P, see Eq. (38) in Appendix A, as:

$$\boldsymbol{\phi}_{E_e}(\mathbf{y}; \mathbf{u}_{e,1}, \dots, \mathbf{u}_{e,n_p}) = \sum_{i=1}^{n_p} \boldsymbol{\varphi}(\mathbf{u}_i) N_i(\mathbf{y}),$$

being $\mathbf{u}_{e,1}, \dots, \mathbf{u}_{e,n_p}$ the parametric coordinates of the nodes of element E_e^P. Thus, the distortion measure at a point $\mathbf{y}$ of an element E_e^I of $\mathcal{M}_I$ can be written as:

$$\mathrm{M}\boldsymbol{\phi}_{E_e}(\mathbf{y}) = \mathrm{M}\boldsymbol{\phi}_{E_e}(\mathbf{y}; \mathbf{u}_{e,1}, \dots, \mathbf{u}_{e,n_p}), \tag{24}$$

where the pairs (e, j) in $\mathbf{u}_{e,j}$ identify the local j-th node of element e with their global mesh number i. That is, for nodal high-order elements, determining ϕ_h^* in the minimization presented in Eq. (23), is equivalent to determining the configuration of the nodes of the high-order mesh. Moreover, the element contribution to the objective function only depends on the nodes of that element.

According to the reasoning above, the optimization problem presented in Eq. (23) can be expressed in such a manner that the nodal parametric coordinates are the unknowns of the problem (free nodes). To this end, we reorder the coordinates of the nodes, $\mathbf{u}_i$, selecting $i = 1, \dots, n_F$ as the indexes corresponding to the inner nodes, and $i = n_F + 1, \dots, n_N$ as the indexes corresponding to the fixed nodes (nodes on the curves of the CAD surfaces). Note that the coordinates of the fixed nodes are determined by the function g_h, and have been computed using the arc-parameter of the corresponding curve of the CAD geometry. Defining

$$f(\mathbf{u}_1, \dots, \mathbf{u}_{n_F}; \mathbf{u}_{n_F+1}, \dots, \mathbf{u}_{n_N}) := \frac{1}{2} \|\mathrm{M}\phi_h - 1\|^2_{\mathcal{M}_I}, \tag{25}$$

we can formulate the mesh optimization problem as finding $\{\mathbf{u}_1^*, \dots, \mathbf{u}_{n_F}^*\}$ in $\mathcal{V} \subset \mathbb{R}^2$ such that:

$$\{\mathbf{u}_1^*, \dots, \mathbf{u}_{n_F}^*\} = \underset{\mathbf{u}_1, \dots, \mathbf{u}_{n_F} \in \mathbb{R}^3}{\operatorname{argmin}} f(\mathbf{u}_1, \dots, \mathbf{u}_{n_F}; \mathbf{u}_{n_F+1}, \dots, \mathbf{u}_{n_N}), \tag{26}$$

where $\mathbf{u}_i = \boldsymbol{\varphi}^{-1}(g_h(\mathbf{y}_i))$ for $i = n_F + 1, \dots, n_N$. In Appendix B, we detail a local approach to solve the global minimization problem stated in Eq. (26).

Note that the optimal configuration is found between the candidates for the minimization presented in Eq. (26). The candidates are the critical coordinates $(\mathbf{u}_1, \dots, \mathbf{u}_{n_F})$ of f, characterized by

$$\frac{\partial f}{\partial \mathbf{u}_i}(\mathbf{u}_1, \dots, \mathbf{u}_{n_F}; \mathbf{u}_{n_F+1}, \dots, \mathbf{u}_{n_N}) = 0, \; i = 1, \dots, n_F. \tag{27}$$

5.4. Independence on the surface parameterization

In this section, we first prove that the defined point-wise measure is independent of the surface parameterization.

Proposition 1 (Independence on the parameterization)
Let $\boldsymbol{\varphi}_1 : \mathcal{V}_1 \to \Sigma_P$ and $\boldsymbol{\varphi}_2 : \mathcal{V}_2 \to \Sigma_P$ be two different diffeomorphic parameterizations of Σ_P. Let $\mathcal{M}$ be a mesh on Σ_P, and E^P an element with the nodes on the surface. Then, the point-wise distortion measure M, presented in Eq. (10), is independent of the surface parameterization.

Proof
Each parameterization $\boldsymbol{\varphi}_j$ with $j = 1, 2$ defines a different function set $\boldsymbol{\mathcal{W}}^j$, see Eq. (15). In particular, for each one of these parameterizations, there exists a set of nodal parametric coordinates $\mathbf{u}^j_{i=1,\dots,n_p}$ in $\mathcal{V}_j$, according to Eq. (38), such that we can write two different mappings $\boldsymbol{\phi}^j_E$ in $\boldsymbol{\mathcal{W}}^{\boldsymbol{j}}_{\boldsymbol{E^I}}$, see Eq. (16):

$$\boldsymbol{\phi}^j_E(\mathbf{y}) = \sum_{i=1}^{n_p} \boldsymbol{\varphi}_j(\mathbf{u}^j_i) N_i(\mathbf{y}), \;\; \mathbf{y} \in E^I, \;\; j = 1, 2.$$

Since both parameterizations are diffeomorphisms, we can write the element nodes $\mathbf{x}_1, \ldots, \mathbf{x}_{n_p}$ of an element E^P as

$$\mathbf{x}_i = \boldsymbol{\varphi}_1(\mathbf{u}_i^1) = \boldsymbol{\varphi}_2(\mathbf{u}_i^2)$$

for unique $\mathbf{u}_i^j$ in $\mathcal{V}_j,\ j = 1, 2,\ i = 1, \ldots, n_p$. Moreover, at any point $\mathbf{y}$ in E^I:

$$\begin{aligned} \boldsymbol{\phi}_E^1(\mathbf{y}) &= \sum_{i=1}^{n_p} \boldsymbol{\varphi}_1(\mathbf{u}_i^1) N_i(\mathbf{y}) \\ &= \sum_{i=1}^{n_p} \mathbf{x}_i N_i(\mathbf{y}) \\ &= \sum_{i=1}^{n_p} \boldsymbol{\varphi}_2(\mathbf{u}_i^2) N_i(\mathbf{y}) = \boldsymbol{\phi}_E^2(\mathbf{y}). \end{aligned} \tag{28}$$

Note that $\boldsymbol{\phi}_E^j$ is $\boldsymbol{\phi}_P^j \circ (\boldsymbol{\phi}_I^j)^{-1}$, see Appendix A. Analogously to Eq. (28), the mappings $\boldsymbol{\phi}_I^j$ and $\boldsymbol{\phi}_P^j$ (between the master and the ideal and physical triangles, respectively) are independent of the CAD parameterization. Next, we denote by M_j the point-wise distortion measure defined using the set $\boldsymbol{\mathcal{W}}_{\boldsymbol{E^I}}^{\boldsymbol{j}}$. Note that M_j in Eq. (10) is strictly determined from $\mathbf{D}\boldsymbol{\phi}_I^j$ and $\mathbf{D}\boldsymbol{\phi}_P^j$. Moreover, since $\boldsymbol{\phi}_I^j$ and $\boldsymbol{\phi}_P^j$ are independent on the parameterization, so their Jacobians are. Therefore, from Eqs. (10) and (24),

$$\mathrm{M}_1\boldsymbol{\phi}_E^1(\mathbf{y}; \mathbf{u}_1^1, \ldots, \mathbf{u}_{n_p}^1) \quad = \quad \mathrm{M}_2\boldsymbol{\phi}_E^2(\mathbf{y}; \mathbf{u}_1^2, \ldots, \mathbf{u}_{n_p}^2).$$

Thus, the distortion at a point $\mathbf{y}$ in E^I is independent of the selected surface parameterization. □

Second, since the conditions imposed for the optimization procedure in Eq. (27) are expressed in terms of M, which is independent of the surface parameterization, we can prove the following result:

Proposition 2
According to the objective function f, defined in Eq. (26), the optimal location for the mesh nodes $\mathbf{x}_i = \boldsymbol{\varphi}(\mathbf{u}_i)$ in $\Sigma,\ i = 1, \ldots, n_F$, is independent of the surface parameterization.

Proof
The conditions for the critical points of f are expressed in terms of M and its derivatives, Eq. (27). Since M is independent of the surface parameterization, Proposition 1, the critical points of f are also independent of the surface mesh parameterization. To finalize, the optimal configurations are also independent of the surface parameterization, since they are found between the candidate configurations. □

Remark 1
In Proposition 2, we have proved that the candidate configurations are independent of the surface parameterization. In particular, the candidate configurations have to be the same for high (smooth Jacobian) and low (highly varying Jacobian) quality surface parameterizations. Therefore, the proposed method is well-suited to obtain candidate mesh configurations even on CAD surfaces represented by low-quality parameterizations.

Remark 2
The goal of the proposed method is to obtain the critical points independently of the surface parameterization. However, there are meshes that cannot be untangled by the proposed method, such as when the boundary edges of the mesh present self-intersections. Nevertheless, the proposed method has properly smoothed and untangled all the tested meshes with valid boundary configurations.

6. DISTORTION AND QUALITY MEASURES FOR HIGH-ORDER ELEMENTS ON SURFACES

To validate the suitability of a given surface mesh for numerical simulation, in this section, we use the point-wise distortion measure presented in Eq. (10) to propose a definition of distortion (quality) for high-order elements.

Definition 1
The *distortion measure for a high-order surface element* is

$$\eta_{\mathcal{V}}^{E} := \frac{\|\mathrm{M}\boldsymbol{\phi}_E\|_{E^I}}{\|1\|_{E^I}}, \tag{29}$$

where $\eta_{\mathcal{V}}^{E}$ is a function of the parametric coordinates of the element nodes $\mathbf{u}_1, \dots, \mathbf{u}_{n_p}$, since $\mathrm{M}\boldsymbol{\phi}_E$ is. Note that $\|1\|_{E^I}$ is the area of the ideal element.

Definition 2
The *quality measure for a high-order surface element* is

$$q_{\mathcal{V}}^{E} := \frac{1}{\eta_{\mathcal{V}}^{E}}. \tag{30}$$

Remark 3
Since $\eta_{\mathcal{V}}^{E}$ is defined in terms of $\mathrm{M}\boldsymbol{\phi}_E$, it is also independent of the selected surface parameterization. Analogously, the corresponding quality measure $q_{\mathcal{V}}^{E}$ is also independent.

To check that the mesh is valid to perform a numerical simulation, a quality measure has to properly detect if an element it is non-valid (and assign 0 value). Moreover, the measure has to penalize the deviation of the element with respect to the target ideal (and assign value 1 to the ideal).

Herein, when we validate a given curved high-order surface mesh, we disable the regularization of the distortion measure, introduced in Eq. (5), by setting δ to 0 in Eq. (10). Therefore, if there is a region where the Jacobian is non-positive ($\sigma \leq 0$), then η_E, Eq. (29), is divergent and the quality $q_{\mathcal{V}}^{E}$ is 0. Conversely, if the physical element is the ideal, $\boldsymbol{\phi}_E$ is the identity. Then, the point-wise distortion $\mathrm{M}\boldsymbol{\phi}_E(\mathbf{y})$ is 1 for all $\mathbf{y} \in E^I$. Thus, by Definition 1, the element distortion η_E is also 1. Summarizing, we state the following remark:

Remark 4
The distortion measure $\eta_{\mathcal{V}}^{E}$ for high-order surface elements has image $[1, \infty)$, where 1 corresponds to the ideal configuration and ∞ to a non-valid one. Hence, by Definition 2, $q_{\mathcal{V}}^{E}$ has image $[0, 1]$, where 0 corresponds to an invalid element, and 1 to the ideal one.

7. EXAMPLES

This section is divided in two parts. First, we present three examples to demonstrate the properties of the proposed smoothing and untangling procedure for nodal high-order meshes with the nodes on CAD geometries. Second, we present three additional examples to illustrate the proposed *a posteriori* approach for generating high-order meshes on CAD surfaces.

We highlight that, in all the figures, the mesh elements are colored according to the quality measure presented in Definition 2. Moreover, for all the examples we present a table summarizing the quality statistics of the mesh elements. Specifically, we provide: the minimum, the maximum, the mean and the standard deviation (SD) of the mesh quality, and the number of tangled elements. In all cases, the smoothed mesh increases the minimum and mean values of the mesh quality and decreases its standard deviation. In all the examples, the resulting high-order elements are valid and curved, and we ensure that the nodes lie on the exact CAD geometry.

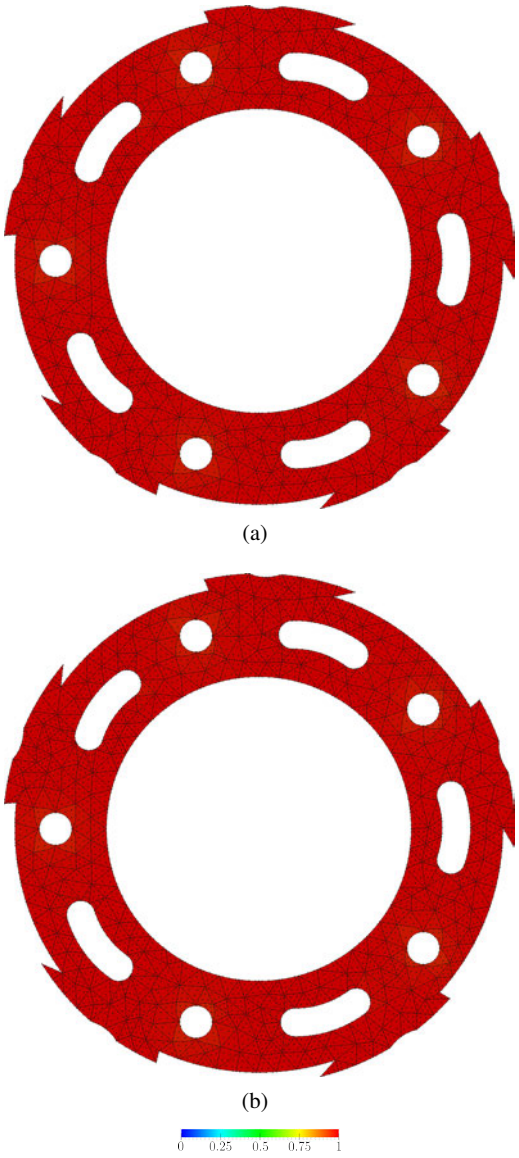

(a)

(b)

Figure 7. Optimization of a planar mesh of degree 3 for a component of a motorbike brake using: (a) the planar technique, and (b) the surface technique.

Mesh	Min	Max	Mean	SD	Tang.
Initial	0.00	1.00	0.98	0.11	6
Fig. 7(a)	0.96	1.00	0.99	0.01	0
Fig. 7(b)	0.96	1.00	0.99	0.01	0

Table I. Shape quality statistics for the high-order meshes on a component of a motorbike brake, presented in Figure 7.

7.1. Properties

In this section, we present three examples to illustrate the main properties of the defined quality measure and the derived optimization process, namely: consistency, independence on the surface parameterization, and robustness of the untangling procedure.

Srf.	Fig.	Min.Q.	Max.Q.	Mean Q.	SD	Tang.
$\boldsymbol{\varphi}^1_{\Sigma_1}$	8(b)	0.29	0.96	0.67	0.18	0
	8(d)	1.00	1.00	1.00	0.00	0
$\boldsymbol{\varphi}^1_{\Sigma_2}$	8(f)	0.43	1.00	0.65	0.16	0
	8(h)	1.00	1.00	1.00	0.00	0
$\boldsymbol{\varphi}^1_{\Sigma_2}$	8(j)	0.16	0.93	0.57	0.22	0
	8(l)	0.91	1.00	0.97	0.02	0
$\boldsymbol{\varphi}^2_{\Sigma_2}$	8(n)	0.34	0.96	0.63	0.16	0
	8(p)	0.91	1.00	0.97	0.02	0

Table II. Shape quality statistics of the meshes on Σ_1 and Σ_2, presented in Figure 8.

7.1.1. Consistency The goal of this example is to illustrate that the point-wise distortion measure for high-order meshes on parameterized surfaces presented in Eq. (10), $\eta_\delta(\bar{\mathbf{J}}(\mathbf{D}\phi_I, \mathbf{D}\phi_P))$, when applied to planar surfaces is equivalent to the point-wise distortion measure for high-order planar meshes presented in [51], $\eta_\delta(\mathbf{D}\phi)$, being $\mathbf{D}\phi$ a 2×2 matrix. It is important to point out that this is true by construction. If the considered surface is planar, the matrix $\bar{\mathbf{J}}$, Eq. (9), required to compute the value of the quality measure, corresponds to the matrix $\mathbf{J}$ except by a rotation. Note that we define the high-order measures in terms of Jacobian distortion measures that are invariant under rigid body motions (such as the shape measure, see details in [54]). Therefore, the distortion for surface elements $\eta_\delta(\bar{\mathbf{J}}(\mathbf{D}\phi_I, \mathbf{D}\phi_P))$ is equal to the planar distortion measure $\eta_\delta(\mathbf{J}(\mathbf{D}\phi_I, \mathbf{D}\phi_P)) = \eta_\delta(\mathbf{D}\phi)$.

To illustrate the consistency, we consider a planar CAD model of a component of a motorbike brake, see Figure 7. First, we generate a mesh composed by 643 elements of degree 3 and 5608 nodes. When the mesh is curved to match the boundary geometry, 8 tangled elements appear. Then, we optimize it using the planar, Figure 7(a), and the surface, Figure 7(b), distortion measures. Note that the ideal triangle for each element has been selected as the corresponding straight-sided high-order element in the initial configuration. To check that we obtain equivalent meshes, we compute

$$E = \max_{i=1,\dots,n_F} \frac{\|\mathbf{x}_i^1 - \mathbf{x}_i^2\|}{L} \tag{31}$$

where L is the minimum edge length in the mesh, and $\mathbf{x}_i^1$ and $\mathbf{x}_i^2$ are the coordinates of the free nodes obtained by the planar and the surface measures, respectively. We obtain that $E = 1.3 \cdot 10^{-4}$ and hence, the meshes are equal up to minimization tolerance. Moreover, according to Table I, we obtain the same quality statistics for both meshes.

7.1.2. Independence on the parameterization The aim of this example is to show that the proposed quality measure and the derived optimization procedure are independent of the surface parameterization, see Sec. 5.4. To illustrate this property, we consider two surfaces, and for each one we define two different parameterizations. For both surfaces, Figure 8 presents the meshes on the parametric space (first and third columns) and on the physical space (second and fourth columns). We generate the same parametric mesh for all surfaces and parameterizations. The mesh is structured and composed by 128 elements of degree 3 and 625 nodes. Since we are using structured meshes, we select as the ideal element an isosceles right triangle. All meshes in Figure 8 are colored according to the shape quality of the elements on the physical space.

Surface 1 Given the parameterization

$$\begin{aligned} \boldsymbol{\varphi}_{\Sigma_1} : \mathcal{V}_{\Sigma_1} = [-1,1]^2 \subset \mathbb{R}^2 &\longrightarrow \mathbb{R}^3 \\ (u,v) &\longrightarrow (u,v,0), \end{aligned}$$

we define the surface Σ_1 as $\boldsymbol{\varphi}_{\Sigma_1}(\mathcal{V}_{\Sigma_1})$. Note that this parameterization has a constant Jacobian. We define two different parameterizations for Σ_1:

$$\begin{aligned} \boldsymbol{\varphi}^1_{\Sigma_1} : \mathcal{V}^1_{\Sigma_1} = [-1,1]^2 &\longrightarrow \Sigma_1 \subset \mathbb{R}^3 \\ (u,v) &\longrightarrow (u, v\,\epsilon(u,v), 0), \end{aligned} \tag{32}$$

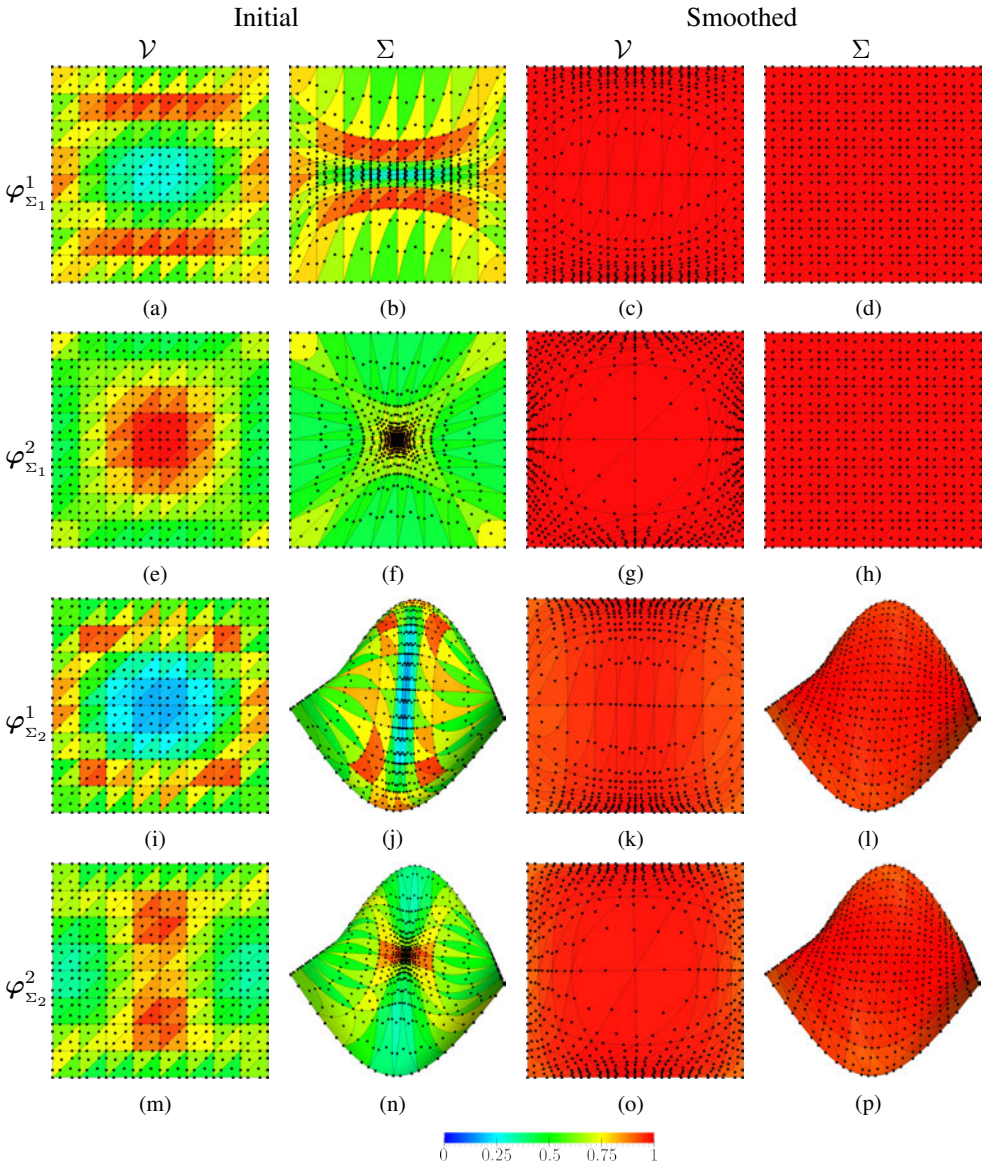

Figure 8. Independence of the optimization procedure on the surface parameterization. Degree three meshes on Σ_1 parameterized by $\boldsymbol{\varphi}^1_{\Sigma_1}$: (a,b) initial meshes on $\mathcal{V}^1_{\Sigma_1}$ and on Σ_1; (c,d) smoothed meshes on $\mathcal{V}^1_{\Sigma_1}$ and on Σ_1. Degree three meshes on Σ_1 parameterized by $\boldsymbol{\varphi}^2_{\Sigma_1}$: (e,f) initial meshes; (g,h) smoothed meshes. Degree three meshes on Σ_2 parameterized by $\boldsymbol{\varphi}^1_{\Sigma_2}$: (i,j) initial meshes; (k,l) smoothed meshes. Degree three meshes on Σ_2 parameterized by $\boldsymbol{\varphi}^2_{\Sigma_2}$: (m,n) initial meshes; (o,p) smoothed meshes.

and

$$\begin{array}{rcl} \boldsymbol{\varphi}^2_{\Sigma_1} : \mathcal{V}^2_{\Sigma_1} = [-1,1]^2 & \longrightarrow & \Sigma_1 \subset \mathbb{R}^3 \\ (u,v) & \longrightarrow & (u\,\epsilon(u,v), v\,\epsilon(u,v), 0), \end{array} \tag{33}$$

where $\epsilon(u,v) := e^{-2(1-u^2)(1-v^2)}$. Note that these parameterizations have a non-constant Jacobian.

The elements of the initial mesh on the parametric space are isosceles right triangles (see Figures 8(a) and 8(e)). These meshes are mapped to the physical space according to $\boldsymbol{\varphi}^1_{\Sigma_1}$ and $\boldsymbol{\varphi}^2_{\Sigma_1}$ respectively, see Figures 8(b) and 8(f). Therefore, the initial meshes on the physical space follow approximately the isolines of the corresponding parameterization. Note that both meshes

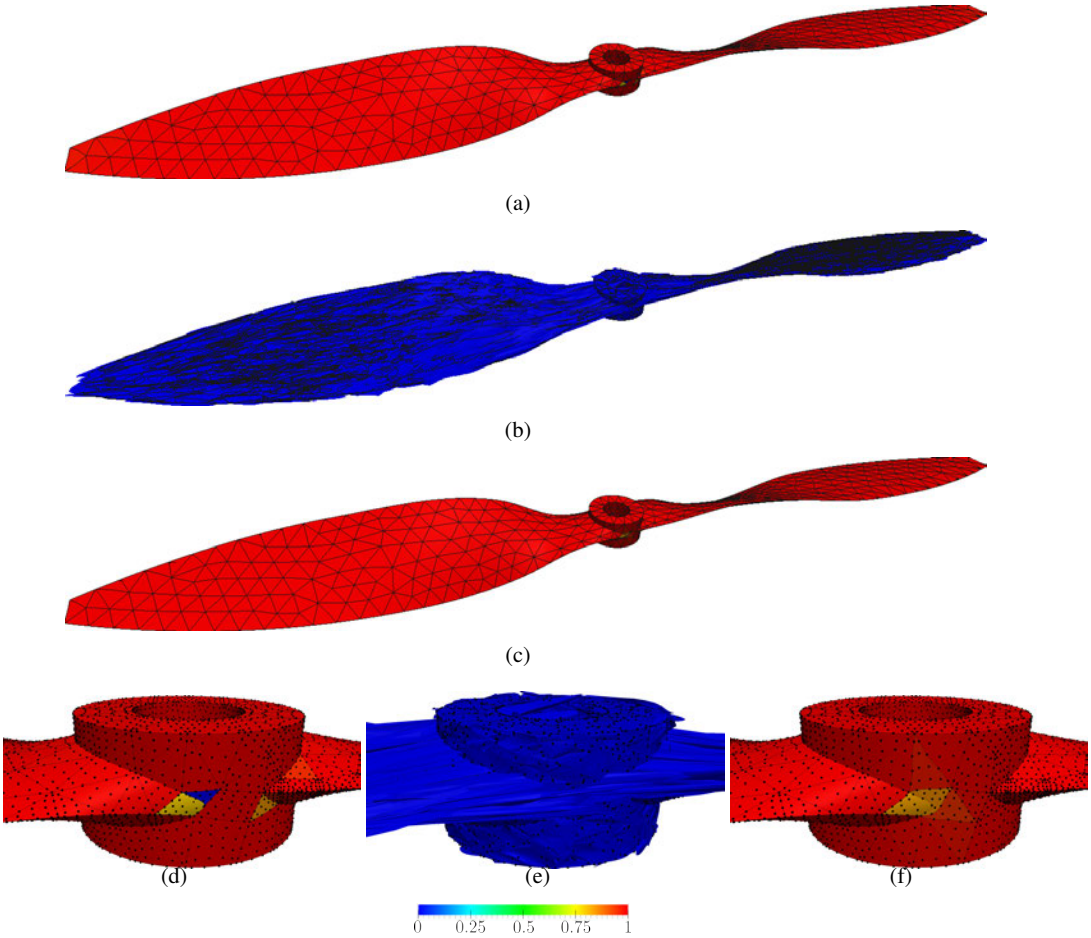

Figure 9. High-order meshes of polynomial degree five colored according to the shape quality measure for a propeller: (a,d) initial curved mesh, (b,e) tangled mesh, and (c,f) smoothed and untangled mesh.

contain low-quality elements due to the use of parameterizations with varying Jacobian matrices. Figures 8(c) and 8(g) show the optimized meshes in the parametric domain, and Figures 8(d) and 8(h) show the optimized meshes on the surface. The distance between both optimized meshes is $E = 1.01 \cdot 10^{-4}$, see Eq. (31). Hence, both meshes are equal up to minimization tolerance.

Surface 2 Given the parameterization

$$\begin{aligned} \boldsymbol{\varphi}_{\Sigma_2} : \mathcal{V}_{\Sigma_2} = [-1,1]^2 \subset \mathbb{R}^2 &\longrightarrow \mathbb{R}^3 \\ (u,v) &\longrightarrow (u, v, \sin(\pi u)\cos(\pi u)). \end{aligned}$$

we define the surface Σ_2 as $\boldsymbol{\varphi}_{\Sigma_2}(\mathcal{V}_{\Sigma_2})$. We define two different parameterizations for Σ_2:

$$\boldsymbol{\varphi}^1_{\Sigma_2}(u,v) := (u, v\ \epsilon(u,v), \sin(\pi u)\ \cos(\pi v\ \epsilon(u,v)))\,,$$

and

$$\begin{aligned} \boldsymbol{\varphi}^2_{\Sigma_2}(u,v) := \quad & (u\ \epsilon(u,v), v\ \epsilon(u,v), \\ & \sin(\pi u\ \epsilon(u,v))\ \cos(\pi v\ \epsilon(u,v))). \end{aligned}$$

In Figures 8(i) and 8(m) we present the structured parametric meshes. The image of these meshes on the surface is presented in Figures 8(j) and 8(n). Again, the parameterizations lead to low quality

Fig.	Min	Max	Mean	SD	Tang.
9(a)	0.00	1.00	1.00	0.04	2
9(b)	0.00	0.23	0.00	0.01	1372
9(c)	0.83	1.00	1.00	0.01	0

Table III. Shape quality statistics of the high-order meshes on a propeller, presented in Figure 9.

meshes on the physical surface. The optimized meshes on the parametric surface are shown in Figures 8(k) and 8(o), and on the physical surface in Figures 8(l) and 8(p). Although in this case we have a non-planar surface, the smoothing-untangling procedure also provides the same meshes up to minimization tolerance with $E = 5.7 \cdot 10^{-4}$.

Table II presents the quality statistics for both surface meshes. The optimization procedure can smooth the initial meshes and obtain a high-quality mesh, increasing significantly in both cases the minimum value of the quality.

7.1.3. Robustness of the smoothing and untangling procedure The goal of this example is to illustrate the capability of the developed procedure to simultaneously untangle and smooth a high-order mesh with a large number of tangled elements. We consider a CAD geometry of a propeller and, according to Sec. 3, we generate an initial mesh of polynomial degree five composed by 1374 elements and 18343 nodes. This non-smoothed mesh contains 2 tangled elements and therefore, is not valid for computational purposes. Figures 9(a) shows a general view of the initial curved high-order mesh, and Figure 9(d) shows a zoom where a tangled element appears. Recall that using the *a posteriori* curving approach detailed in Sec. 3, we normally obtain meshes with several tangled elements when the boundary is curved to match the geometry. These elements are usually located on the boundaries of the surface and therefore, the number of tangled elements is small compared to the total number of elements.

To check the robustness of the untangling capability of the proposed method, we increase the number of tangled elements by applying a random perturbation to the location of the inner nodes of the surface. The resulting mesh contains 1372 tangled elements, see Figures 9(b) and 9(e). After applying the optimization procedure we obtain a high-quality mesh without tangled elements, see Figures 9(c) and 9(f). The ideal triangle for each element is the corresponding straight-sided element in the initial configuration. Table III summarizes the quality statistics of the three high-order meshes. We highlight that the smoothed mesh increases the values of the minimum quality of the initial and randomized meshes.

In addition, we have also smoothed the initial mesh (the mesh with only two tangled elements) and we obtain the same smoothed mesh up to minimization tolerance. Specifically, the relative distances between the smoothed meshes is $E = 1 \cdot 10^{-10}$, see Eq. (31).

7.2. High-order curved meshing

In this section, we analyze several aspects of the proposed *a posteriori* approach to generate high-order meshes on parameterized surfaces, see Sec. 3. First, we illustrate the complete procedure to generate a final valid high-order mesh on a CAD geometry. Next, we show that the proposed methodology is able to generate meshes of low and high polynomial degrees for a given geometry. Finally, we analyze the quality of the obtained meshes in terms of the scaled Jacobian measure, that is a standard measure of the smoothness of the element representation mapping, see [57, 35, 36, 37].

7.2.1. High-order mesh generation on a CAD geometry The objective of this example is to illustrate the complete process for the generation of a high-order mesh on a CAD geometry. We consider a CAD model of a Falcon aircraft and we generate a valid mesh of polynomial degree five. Figure 10 shows each one of the required steps. In the first column, the elements are colored according to the quality that results from considering an equilateral triangle as an ideal element. This corresponds to an absolute value of the quality, since it uses the same ideal for all the elements. In the second column, the elements are colored according to the quality measure that results from considering the

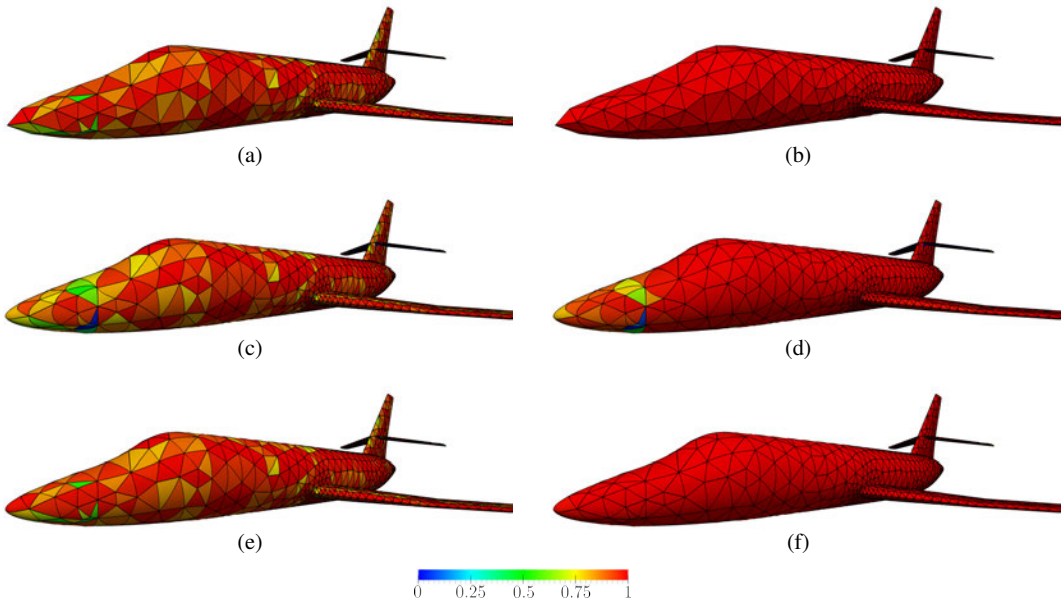

Figure 10. Snap-shots of the meshes involved in the generation of a high-order mesh for a Falcon aircraft: (a,b) initial linear mesh; (c,d) initial curved mesh of polynomial degree five, and (e,f) optimized mesh of polynomial degree five. Figures (a,c,e) are colored taking the ideal as the equilateral triangle. Figures (b,d,f) are colored taking the ideal as the corresponding element in the straight-sided mesh.

p	Fig.	Min	Max	Mean	SD	Tang.
1	10(b)	1.00	1.00	1.00	0.00	0
1	10(a)	0.21	1.00	0.93	0.09	0
5	10(d)	0.00	1.00	0.97	0.14	45
5	10(c)	0.00	1.00	0.91	0.16	45
5	10(f)	0.69	1.00	0.99	0.01	0
5	10(e)	0.24	1.00	0.93	0.09	0

Table IV. Shape quality statistics of the high-order meshes on a Falcon aircraft, presented in Figure 10.

initial straigth-sided high-order elements as ideal elements. This corresponds to a relative value of the quality, since it allows comparing each element to a different ideal triangle determined by the corresponding element in the initial linear mesh.

First, we generate an initial linear mesh using any established mesh generator that provides control over the size and shape of the generated elements, see Figures 10(a) and 10(b). Note that these mesh characteristics will be inherited by the final high-order mesh. Second, we set the ideal mesh increasing the order of the initial straight-sided linear mesh. Thus, for the optimization procedure, the ideal triangle for each element is the corresponding high-order straight-sided triangle in the initial configuration. Third, we get the parametric coordinates of the linear mesh. If we do not have access to them, we use the projection technique presented in [67] to compute them. Next, we increase the polynomial degree of the mesh in the parametric space, and we map it to the CAD surface according to its parameterization, see Figure 10(c) and 10(d). Note that several tangled elements appear. Then, we optimize this mesh on the parametric space, and we map it to the surface. To assess that we obtain a valid high-order mesh composed by elements that preserve the shape of the initial linear mesh we present the optimized mesh in Figures 10(e) and 10(f).

From Figures 10(e) and 10(f), we realize that the quality distribution is similar to the quality distribution of the initial linear mesh. Thus, the mesh does not present the inverted elements of Figure 10(d) and is a valid high-order mesh that preserves, whenever is possible, the shape of the elements of the initial straight-sided high-order mesh.

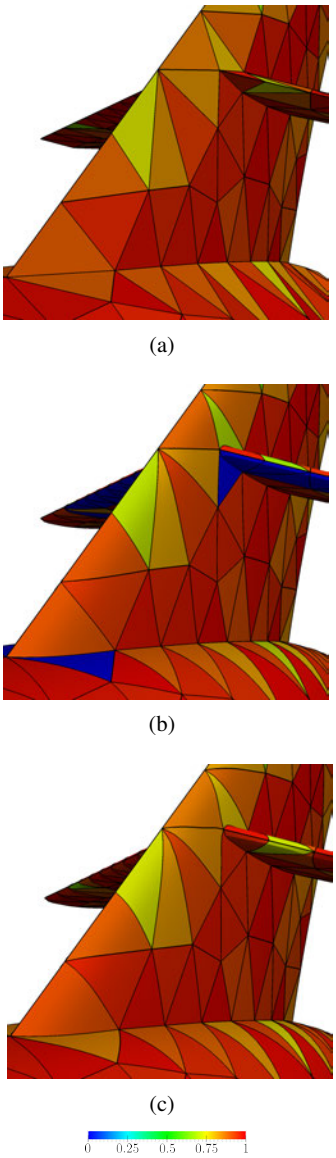

Figure 11. Process of the generation of a high-order mesh on the horizontal stabilizer of a falcon aircraft, colored taking the ideal as the equilateral triangle: (a) linear mesh, (b) initial (invalid) curved mesh of polynomial degree four, and (c) optimized (valid) mesh of polynomial degree four.

Figure 11 illustrates the mesh generation process around the horizontal stabilizer. Figure 11(a) shows the initial linear mesh. Next, Figure 11(b) presents the initial curved mesh of polynomial degree 4 that presents both types of tangling issues illustrated in Figure 2. Finally, Figure 11(c) shows the final mesh resulting from the optimization procedure.

Table IV summarizes the quality values of the meshes presented in this example. Note that the optimized mesh does not include tangled elements. Note that the mean value of the shape quality is 0.99 with a standard deviation of 0.01 when the ideal is selected as the initial linear mesh.

7.2.2. High polynomial degree The aim of this example is to show the capability of the presented methodology to generate valid and high-quality meshes for high polynomial degree. To this end, we first generate an initial linear mesh composed by 832 elements of the CAD geometry of a component of a gear box. Then, we increase the polynomial degree of the initial mesh to degree 3, 5, 8 and 10.

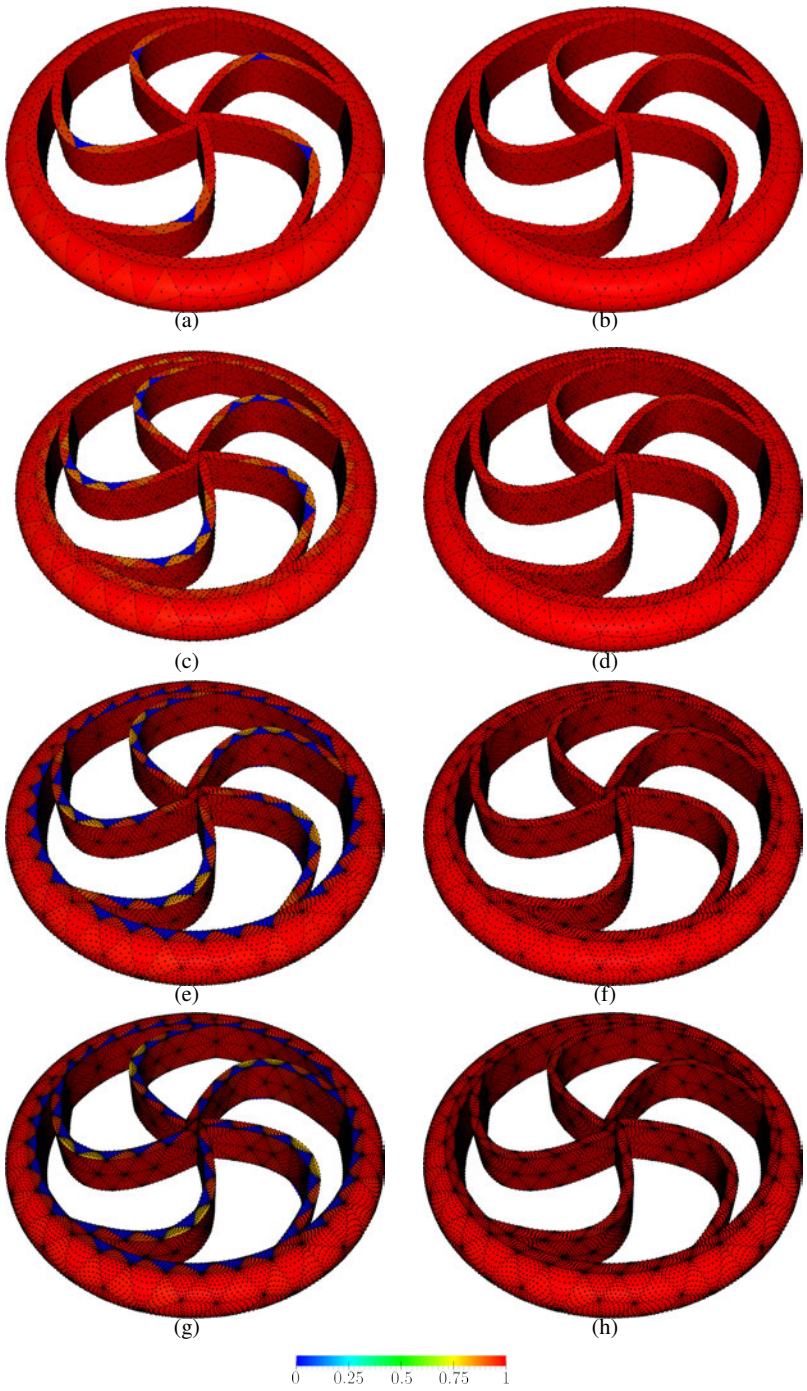

Figure 12. High-order meshes of polynomial degrees 3, 5, 8 and 10 for a component of a gear box. (a,c,e,g) Initial curved meshes. (b,d,f,h) Optimized meshes.

As expected, these meshes contain tangled elements. In the first column of Figure 12, we present the initial high-order meshes. We observe that the number of tangled elements changes depending on the polynomial degree (from 10 tangled elements for degree 3 to 130 tangled elements for degree 10). The number of tangled element increases with the polynomial degree since the feasible region of the nodes of the higher degree elements is smaller. Then, we apply the proposed optimization procedure to each initial high-order mesh, selecting the ideal for each element as the corresponding

p	Fig.	Min	Max	Mean	SD	Tang.
3	12(a)	0.00	1.00	0.98	0.11	10
3	12(b)	0.98	1.00	1.00	0.00	0
5	12(c)	0.00	1.00	0.95	0.19	30
5	12(d)	0.98	1.00	1.00	0.00	0
8	12(e)	0.00	1.00	0.86	0.34	110
8	12(f)	0.98	1.00	1.00	0.00	0
10	12(g)	0.00	1.00	0.83	0.36	130
10	12(h)	0.98	1.00	1.00	0.00	0

Table V. Shape quality statistics of the high-order meshes on a component of a gear box, presented in Figure 12 .

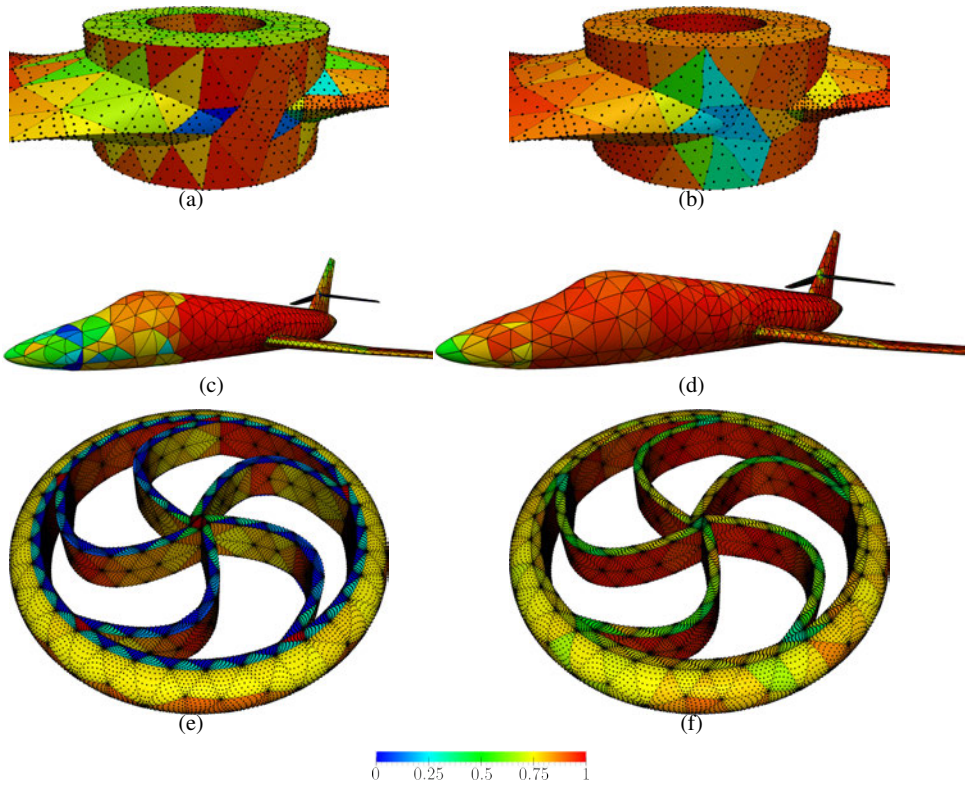

Figure 13. Initial and optimized high-order meshes colored according to the scaled Jacobian quality measure for the examples presented in Sec. 7.2: (a,b) degree 5 meshes on a propeller, (c,d) degree 5 meshes on a Falcon aircraft, and (e,f) degree 10 meshes on a component of a gear box.

element in the initial straight-sided high-order mesh. In the second column of Figure 12 we present the optimized high-order meshes.

Table V details the shape quality statistics of the presented meshes. For any of the tested degrees, the proposed procedure provides a valid and high-quality mesh, obtaining a valid configuration from an invalid initial one.

7.2.3. Validation of the smoothness of the representation mapping In this section, we present an analysis of the scaled Jacobian measure for the degree 5 meshes generated in Secs. 7.1.3 and 7.2.1, and for the degree 10 mesh generated in Sec. 7.2.2. The scaled Jacobian element quality measure

$$J = \frac{\min_{\mathbf{y}\in E^I} \det \bar{\mathbf{J}}(\mathbf{D}\phi_I, \mathbf{D}\phi_P)}{\max_{\mathbf{y}\in E^I} \det \bar{\mathbf{J}}(\mathbf{D}\phi_I, \mathbf{D}\phi_P)} \tag{34}$$

Mesh	Fig.	Min	Max	Mean	Std.Dev.	Tang.
Initial	13(a)	-2.93	1.00	0.89	0.18	2
Smoothed	13(b)	0.18	1.00	0.95	0.08	0
Initial	13(c)	-0.75	1.00	0.85	0.25	50
Smoothed	13(d)	0.09	1.00	0.92	0.11	0
Initial	13(e)	-5.55	1.00	0.36	1.06	130
Smoothed	13(f)	0.26	1.00	0.81	0.16	0

Table VI. Scaled Jacobian element quality statistics of the high-order meshes presented on Figure 13.

is widely used to assess the validity of the high-order mesh elements [57, 35, 36, 37], and it quantifies the variation of the Jacobian of the representation mapping. In fact, it quantifies the *linearity* of the representation mapping, being 1 only for constant Jacobian matrices, that is, for linear elements.

It is important to point out that we expect an improvement on the scaled Jacobian quality measure of the meshes obtained with the proposed optimization procedure. On the one hand, from Eq. (34) we realize that the scaled Jacobian measure is constant for linear elements, and penalizes elements with non-constant Jacobian. On the other hand, we highlight that our approach considers as ideal the initial straight-sided high-order element. Thus, it tries to transform the physical curved element into a high-order element with similar shape to the initial straight-sided one, while it maintains the nodes on the surface.

In Figure 13, we color the meshes presented in the previous examples using the scaled Jacobian quality measure. In the first and second columns of Figure 13 we show the initial and optimized high-order meshes, respectively. In Table VI we display the scaled Jacobian quality statistics for the meshes presented in Figure 13. As expected, using the proposed approach we improve the minimum and the mean values of the scaled Jacobian quality measure in all the cases. Hence, we obtain valid and high-order meshes with a fairly smooth Jacobian of the representation mapping.

8. CONCLUDING REMARKS

The main goal of this work is to validate and generate curved meshes of any polynomial degree on parameterized CAD surfaces. First, we detail a new technique to extend any Jacobian-based distortion (quality) measure defined for planar triangles to high-order elements on parameterized surfaces. The proposed measure is expressed in terms of the parametric coordinates of the mesh nodes, and we prove that it is independent of the surface parameterization.

Second, we develop a continuous optimization procedure to smooth and untangle high-order meshes on parameterized surfaces. Specifically, we propose a non-linear least-squares formulation to enforce in a weak form that the distortion of the mesh is minimal. The optimization procedure is formulated in terms of the parametric coordinates. Thus, it ensures that the nodes always lie on the exact CAD geometry. Moreover, the distortion measure is regularized to allow untangling inverted elements. In particular, the presented regularization technique avoids that a valid element becomes invalid and is capable of untangling meshes composed by a large number of inverted elements.

In addition, we prove that the optimization procedure is independent of the surface parameterization. That is, given two diffeomorphic parameterizations of the surface, the physical candidate locations are the same for both parameterizations. Therefore, this technique is particularly suited to generate high-order meshes on CAD geometries represented by low-quality parameterizations.

Third, we present an *a posteriori* mesh generation procedure for CAD geometries. Specifically, given a linear mesh, we increase the polynomial degree of the elements on the parametric space, and then we improve the quality of the resulting mesh by means of the proposed optimization procedure. Note that it is of the major importance that the optimization procedure allows untangling, since

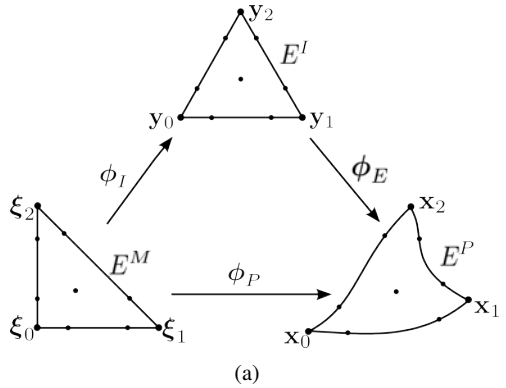

(a)

Figure 14. Mappings between the master, the ideal and the physical high-order elements. Application to nodal high-order triangles.

when the polynomial degree of the elements is increased, more inverted elements appear close to the boundary curves.

To conclude, we have included several examples to show the properties of the presented procedure, and to illustrate the *a posteriori* approach to generate high-order meshes. We present two sets of examples. First, we demonstrate the properties of the presented technique the: consistence, independence of the surface parameterization, and robustness of the untangling technique. Second, we analyze the mesh generation process for CAD geometries. We show a detailed decomposition of the mesh generation process, the capability to generate low and high-order meshes up to degree ten, and a detailed analysis of the meshes obtained on three different CAD models.

Regarding the computational cost of the proposed optimization procedure, the presented method is in general terms more expensive than standard smoothing approaches (without untangling). For instance, the proposed implementation of our method is more expensive than standard node-by-node Laplacian smoothing. That is, the cost of moving a node is also proportional to the number of neighbors, but there are more floating operations involved. Nevertheless, our implementation scales as the node-by-node Laplacian method up to an implementation constant. We highlight that the overhead of our method pays off in those applications where a valid curved high-order surface mesh cannot be obtained with a standard smoothing method that does not feature untangling capabilities. In the near future, we will perform an study of the cost of the optimization, analyzing the number of iterations to converge and the scalability of the solver in terms of the number of elements.

A. NODAL HIGH-ORDER ELEMENTS ON PARAMETERIZED SURFACES

In this section, we detail the selected element representation in $\boldsymbol{\mathcal{W}}$, see Eq. (15). Let E^P in $\mathcal{M}_P$ be a nodal high-order element of polynomial degree p determined by n_p nodes with coordinates $\mathbf{x}_i$ in $\Sigma_P \subset \mathbb{R}^3$, for $i = 1, \ldots, n_p$. Note that for triangular elements the number of nodes n_p is $\frac{1}{2}(p+1)(p+2)$. In addition, to improve the interpolation properties of the obtained high-order elements, we use a node distribution that provides a quasi-optimal Lebesgue constant [4]. Given a master element E^M with nodes $\boldsymbol{\xi}_j$ in $\mathbb{R}^2$, being $j = 1, \ldots, n_p$, we consider the basis $\{\bar{N}_i\}_{i=1,\ldots,n_p}$ of nodal interpolative shape functions (Lagrange interpolation) of degree p. Then, the high-order representation mapping from E^M to E^P, see Figure 14, can be expressed as:

$$\begin{aligned} \boldsymbol{\phi}_P : E^M \subset \mathbb{R}^2 &\longrightarrow E^P \subset \mathbb{R}^3 \\ \boldsymbol{\xi} &\longmapsto \mathbf{x} = \boldsymbol{\phi}_P(\boldsymbol{\xi}) = \sum_{i=1}^{n_p} \mathbf{x}_i \bar{N}_i(\boldsymbol{\xi}). \end{aligned} \tag{35}$$

Note that $\boldsymbol{\phi}_P(\boldsymbol{\xi})$ can be written as $\boldsymbol{\phi}_P(\boldsymbol{\xi}; \mathbf{x}_1, \dots, \mathbf{x}_{n_p})$, since it also depends on the node coordinates $\mathbf{x}_1, \dots, \mathbf{x}_{n_p}$. Moreover, recall that the shape functions $\{\bar{N}_i\}_{i=1,\dots,n_p}$ depend on the selection of $\boldsymbol{\xi}_j$, for $j = 1, \dots, n_p$. In addition, they form a partition of the unity on E^M, and hold that $\bar{N}_i(\boldsymbol{\xi}_j) = \delta_{ij}$, for $i, j = 1, \dots, n_p$.

Analogously, the mapping $\boldsymbol{\phi}_I$ between the master and the ideal elements is also determined using nodal high-order shape functions. Recall that, in this work, we set the elements of the ideal mesh to be high-order, and straight-sided. Hence, we can write $\boldsymbol{\phi}_I$ as:

$$\begin{aligned} \boldsymbol{\phi}_I : E^M \subset \mathbb{R}^2 &\longrightarrow E^I \subset \mathbb{R}^3 \\ \boldsymbol{\xi} &\longmapsto \mathbf{y} = \boldsymbol{\phi}_I(\boldsymbol{\xi}) = \sum_{i=1}^{n_p} \mathbf{y}_i \bar{N}_i(\boldsymbol{\xi}). \end{aligned} \tag{36}$$

Note that, since E^I is straight-sided, $\boldsymbol{\phi}_I$ is an affine mapping with a constant Jacobian matrix.

Finally, the mapping between the ideal and physical elements can be written as:

$$\begin{aligned} \boldsymbol{\phi}_E : E^I \subset \mathbb{R}^3 &\longrightarrow E^P \subset \mathbb{R}^3 \\ \mathbf{y} &\longmapsto \mathbf{x} = \boldsymbol{\phi}_E(\mathbf{y}) = \boldsymbol{\phi}_P \circ \boldsymbol{\phi}_I^{-1}(\mathbf{y}) \\ &= \sum_{i=1}^{n_p} \mathbf{x}_i \bar{N}_i(\boldsymbol{\phi}_I^{-1}(\mathbf{y})) = \sum_{i=1}^{n_p} \mathbf{x}_i N_i(\mathbf{y}). \end{aligned} \tag{37}$$

where $N_i(\mathbf{y}) := \bar{N}_i(\boldsymbol{\phi}_I^{-1}(\mathbf{y}))$, is an interpolative shape function of polynomial degree p on E^I, since $\boldsymbol{\phi}_I$ is an affine mapping.

Note that $\boldsymbol{\phi}_E(\mathbf{y})$ can be written as $\boldsymbol{\phi}_E(\mathbf{y}; \mathbf{x}_1, \dots, \mathbf{x}_{n_p})$, since it also depends on the node coordinates $\mathbf{x}_1, \dots, \mathbf{x}_{n_p}$. Moreover, the nodes on the surface can be expressed in terms of the parametric coordinates by means of the surface parameterization $\boldsymbol{\varphi}$, see Eq. (1). Hence, for a surface element, the mapping $\boldsymbol{\phi}_E$ can also be expressed in terms of the parametric coordinates of the element nodes as

$$\boldsymbol{\phi}_E(\mathbf{y}; \mathbf{x}_1, \dots, \mathbf{x}_{n_p}) = \boldsymbol{\phi}_E(\mathbf{y}; \boldsymbol{\varphi}(\mathbf{u}_1), \dots, \boldsymbol{\varphi}(\mathbf{u}_{n_p})).$$

In this manner, for optimization purposes, the nodes can be moved on the parametric space keeping the physical location always on the surface. Specifically, the mapping between the ideal and physical elements can be rewritten as:

$$\begin{aligned} \boldsymbol{\phi}_E : E^I \subset \mathbb{R}^3 &\longrightarrow E^P \subset \mathbb{R}^3 \\ \mathbf{y} &\longmapsto \mathbf{x} = \sum_{i=1}^{n_p} \boldsymbol{\varphi}(\mathbf{u}_i) N_i(\mathbf{y}), \end{aligned} \tag{38}$$

It is important to point out that $\boldsymbol{\phi}_E$ is in $\boldsymbol{\mathcal{W}_{E^I}}$, see Eq. (16). Specifically, we express ϕ_h element-wise as $\phi_{h|E^P} = \boldsymbol{\phi}_E$. Hence, the polynomial mesh representation ϕ_h is in $\boldsymbol{\mathcal{W}}$.

Remark 5

We choose E^I as a valid straight-sided high-order triangle. That is, $\boldsymbol{\phi}_I$ is an invertible affine mapping and therefore, a global diffeomorphism. In this way, we can use the change of variable determined by $\boldsymbol{\phi}_I$ to compute the inner product, Eq. (21), as:

$$\langle f, g \rangle_{E^I} := \int_{E^M} f(\boldsymbol{\phi}_I(\boldsymbol{\xi}))\, g(\boldsymbol{\phi}_I(\boldsymbol{\xi})) \left\| \frac{\partial \boldsymbol{\phi}_I}{\partial \boldsymbol{\xi}_1} \times \frac{\partial \boldsymbol{\phi}_I}{\partial \boldsymbol{\xi}_2} \right\|. \tag{39}$$

To compute this integral, we have to use a numerical quadrature that ensures that polynomials of degree $6p - 3$ are integrated exactly. Specifically, the quadrature uses $(q + 1)(q + 2)/2$ integration points, where $q = 3p - 2$, as specified in [13, 14].

B. IMPLEMENTATION: SUBMESH DISTORTION

To solve the optimization problem in Eq. (26), we have to find the optimum between the candidate configurations. These configurations are characterized by the global non-linear constraints in Eq. (27). To solve these constraints, we choose a non-linear iterative method that: exploits the locality of the problem, avoids solving large linear systems, and is well suited for parallelization (by coloring the mesh nodes). Specifically, we use a non-linear iterative Gauss-Seidel method determined by the iteration

$$\mathbf{u}_i^{k+1} = \mathbf{u}_i^k - \alpha_i^k \, [\boldsymbol{\nabla}_{ii}^2 f(\mathbf{w}_i^k)]^{-1} \, \boldsymbol{\nabla}_i f(\mathbf{w}_i^k) \qquad i = 1, \dots, n_F, \tag{40}$$

where α_i^k is the step length, and

$$\mathbf{w}_i^k = (\mathbf{u}_1^{k+1}, \dots, \mathbf{u}_{i-1}^{k+1}, \mathbf{u}_i^k, \mathbf{u}_{i+1}^k, \dots, \mathbf{u}_{n_F}^k; \mathbf{u}_{n_F+1}^0, \dots, \mathbf{u}_{n_N}^0)$$

is the vector of updated node locations for the $i-1$ first nodes. Note that $\boldsymbol{\nabla}_i$ and $\boldsymbol{\nabla}_{ii}^2$ denote the gradient and the Hessian with respect to the coordinates $\mathbf{u}_i$ of node i.

To implement this iterative non-linear solver, we have to compute the gradient $\boldsymbol{\nabla}_i f$, the Hessian $\boldsymbol{\nabla}_{ii}^2 f$, and the step length, α_i^k. We first observe that the computation of the gradient

$$\boldsymbol{\nabla}_i f(\mathbf{u}_1, \dots, \mathbf{u}_{n_F}; \mathbf{u}_{n_F+1}, \dots, \mathbf{u}_{n_N}) = \frac{\partial}{\partial \mathbf{u}_i} \sum_{j=1}^{n_E} f_{E_j}(\mathbf{u}_{j,1}, \dots, \mathbf{u}_{j,n_p}),$$

can be simplified. That is, f_{E_j} only depends on the coordinates of the nodes of the element E_j. Therefore, we have that $\frac{\partial}{\partial \mathbf{u}_i} f_{E_j} = 0$ for all the elements j that do not contain the node i. Thus, the gradient can be evaluated as

$$\boldsymbol{\nabla}_i f(\mathbf{u}_1, \dots, \mathbf{u}_{n_F}; \mathbf{u}_{n_F+1}, \dots, \mathbf{u}_{n_N}) = \sum_{j \sim i} \frac{\partial}{\partial \mathbf{u}_i} f_{E_j}(\mathbf{u}_{j,1}, \dots, \mathbf{u}_{j,n_p}),$$

where $j \sim i$ denotes that the summation is performed only for the elements that contain the node i. Therefore, if we define

$$\hat{f}(\mathbf{u}_i) := \sum_{j \sim i} f_{E_j}(\mathbf{u}_{j,1}, \dots, \mathbf{u}_{j,n_p}), \tag{41}$$

we have that

$$\boldsymbol{\nabla}_i f(\mathbf{u}_1, \dots, \mathbf{u}_{n_F}; \mathbf{u}_{n_F+1}, \dots, \mathbf{u}_{n_N}) = \boldsymbol{\nabla}_i \hat{f}(\mathbf{u}_i) \tag{42}$$

Moreover, using a similar reasoning the Hessian can be computed as

$$\boldsymbol{\nabla}_{ii}^2 f(\mathbf{u}_1, \dots, \mathbf{u}_{n_F}; \mathbf{u}_{n_F+1}, \dots, \mathbf{u}_{n_N}) = \boldsymbol{\nabla}_{ii}^2 \hat{f}(\mathbf{u}_i) \tag{43}$$

Finally, we have to compute the step length α_i^k. To this end, we use the Backtracking Line Search algorithm [70] detailed in Algorithm 1, where we set: $\alpha = 1$, $\rho = 0.5$ and $c = 10^{-4}$. Note that in this algorithm, we have to evaluate the global objective function f and its gradient to check the sufficient decrease condition in Line 4. By Eq. (42), the sufficient decrease condition is equivalent to

$$f(\mathbf{w}_i^\alpha) > f(\mathbf{w}_i^k) + c\alpha [\boldsymbol{\nabla}_i \hat{f}(\mathbf{u}_i^k)]^T \mathbf{p}_i^k,$$

where $\mathbf{w}_i^\alpha$ is defined in Line 3 of Algorithm 1. Moreover, we have that

$$f(\mathbf{w}_i^\alpha) - f(\mathbf{w}_i^k) = \hat{f}(\mathbf{u}_i^\alpha) - \hat{f}(\mathbf{u}_i^k),$$

Algorithm 1 Backtracking Line Search

function BACKLINESEARCH(Vector $\mathbf{w}_i^k$, Vector $\mathbf{p}_i^k$)
  Set $\alpha > 0,\ \rho \in (0,1),\ c \in (0,1)$;
  $\mathbf{w}_i^\alpha \leftarrow \mathbf{w}_i^k + (\mathbf{0},\dots,\mathbf{0},\alpha\mathbf{p}_i^k,\mathbf{0},\dots,\mathbf{0})$;
  while $f(\mathbf{w}_i^\alpha) > f(\mathbf{w}_i^k) + c\alpha[\boldsymbol{\nabla}_i f(\mathbf{w}_i^k)]^T\mathbf{p}_i^k$ **do**
    $\alpha \leftarrow \rho\alpha$;
    $\mathbf{w}_i^\alpha \leftarrow \mathbf{w}_i^k + (\mathbf{0},\dots,\mathbf{0},\alpha\mathbf{p}_i^k,\mathbf{0},\dots,\mathbf{0})$;
  end while
  return α;
end function

since the contributions of the elements that do not depend on the free node are mutually cancelled, being $\mathbf{u}_i^\alpha = \mathbf{u}_i^k + \alpha\mathbf{p}_i^k$. Therefore, the sufficient decrease condition is equivalent to

$$\hat{f}(\mathbf{u}_i^\alpha) > \hat{f}(\mathbf{u}_i^k) + c\alpha[\boldsymbol{\nabla}_i\hat{f}(\mathbf{u}_i^k)]^T\mathbf{p}_i^k. \tag{44}$$

Taking into account Eqs. (42), (43), and (44), we conclude that in the implementation we only need to compute the gradients, the Hessian, and the value of the local function $\hat{f}$ introduced in Eq. (41).

In our implementation, we exploit the computational reduction associated with the evaluation of the function $\hat{f}$. To this end, we denote by $\mathcal{M}_\mathbf{u}$ the elements that contain a free node $\mathbf{u}$. The set of elements $\mathcal{M}_\mathbf{u}$ is referred as the *submesh* associated with node $\mathbf{u}$. In the following remark, we use this notation to reinterpret the local function $\hat{f}$ as a measure of the deviation of the submesh distortion respect an ideal configuration. In addition, we state the optimized implementation for the non-linear iterative method.

Remark 6
Let $\mathbf{u}_i^k$ be the coordinates of node i at step k, and let $\mathcal{M}_{\mathbf{u}_i^k}$ be the corresponding associated submesh composed by m_i elements. We say that $\hat{f}(\mathbf{u}_i)$, defined in Eq. (41), is a local merit function that measures the *deviation respect an ideal configuration of the submesh distortion associated with* $\mathbf{u}_i$. According to this merit function, and to Eqs. (42), (43), and (44), we can implement the iteration $k+1$ for node i of the proposed non-linear method, Eq. (40), as

$$\mathbf{u}_i^{k+1} = \mathbf{u}_i^k - \alpha_i^k\ [\boldsymbol{\nabla}_{ii}^2\hat{f}(\mathbf{u}_i^k)]^{-1}\ \boldsymbol{\nabla}_i\hat{f}(\mathbf{u}_i^k) \qquad i = 1,\dots,n_F. \tag{45}$$

References

1. B. Szabó, I. Babuška, Finite Element Analysis, John Wiley & Sons New York, 1991.
2. C. Schwab, p-and hp-finite element methods: Theory and applications in solid and fluid mechanics, Clarendon Press Oxford, 1998.
3. M. O. Deville, P. F. Fischer, E. H. Mund, High-order methods for incompressible fluid flow, Vol. 9, Cambridge University Press, 2002.
4. J. Hesthaven, T. Warburton, Nodal Discontinuous Galerkin Methods: Algorithms, Analysis, and Applications, Texts in Applied Mathematics, Springer, 2007.
5. G. Karniadakis, S. Sherwin, Spectral/hp element methods for computational fluid dynamics, Oxford University Press, 2013.
6. I. Babuška, B. Szabó, I. Katz, The p-version of the finite element method, SIAM J. Numer. Anal. 18 (1981) 515–545.
7. P. E. Vos, S. Sherwin, R. Kirby, From h to p efficiently: implementing finite and spectral/hp element methods to achieve optimal performance for low- and high-order discretisations, J. Comput. Phys. 229 (13) (2010) 5161–5181.
8. C. Cantwell, S. Sherwin, R. Kirby, P. Kelly, From h to p efficiently: strategy selection for operator evaluation on hexahedral and tetrahedral elements, Comput. Fluids 43 (1) (2011) 23–28.
9. C. Cantwell, S. Sherwin, R. Kirby, P. Kelly, From h to p efficiently: selecting the optimal spectral/hp discretisation in three dimensions, Math. Model. Nat. Phenom. 6 (3) (2011) 84–96.
10. R. Löhner, Error and work estimates for high-order elements, Int. J. Numer. Meth. Fluids 67 (12) (2011) 2184–2188.
11. M. Yano, et al., An optimization framework for adaptive higher-order discretizations of partial differential equations on anisotropic simplex meshes, Ph.D. thesis, Massachusetts Institute of Technology (2012).
12. R. Kirby, S. Sherwin, B. Cockburn, To CG or to HDG: a comparative study, J. Sci. Comput. 51 (1) (2012) 183–212.

13. A. Huerta, X. Roca, A. Angeloski, J. Peraire, Are high-order and hybridizable discontinuous Galerkin methods competitive?, Oberwolfach Rep. 9 (1) (2012) 485 – 487.
14. A. Huerta, A. Angeloski, X. Roca, J. Peraire, Efficiency of high-order elements for continuous and discontinuous Galerkin methods, Int. J. Numer. Meth. Eng. 96 (2013) 529–560. doi:10.1002/nme.4547.
15. R. Löhner, Improved error and work estimates for high-order elements, Int. J. Numer. Meth. Fluids 72 (2013) 1207–1218.
16. Z. Wang, K. Fidkowski, R. Abgrall, F. Bassi, D. Caraeni, A. Cary, H. Deconinck, R. Hartmann, K. Hillewaert, H. Huynh, et al., High-order cfd methods: current status and perspective, Int. J. Numer. Meth. Fluids 72 (8) (2013) 811–845.
17. D. Dawe, High-order triangular finite element for shell analysis, Int. J. Solids Struct. 11 (10) (1975) 1097–1110.
18. A. Peano, Efficient high order finite elements for shells, Meccanica 11 (1) (1976) 42–47.
19. F. Cirak, M. Ortiz, P. Schroder, Subdivision surfaces: a new paradigm for thin-shell finite-element analysis, Int. J. Numer. Meth. Eng. 47 (12) (2000) 2039–2072.
20. T. Hughes, J. A. Cottrell, Y. Bazilevs, Isogeometric analysis: Cad, finite elements, nurbs, exact geometry and mesh refinement, Comput. Meth. Appl. Mech. Eng. 194 (39) (2005) 4135–4195.
21. J. Kiendl, K.-U. Bletzinger, J. Linhard, R. Wüchner, Isogeometric shell analysis with kirchhoff–love elements, Comput. Meth. Appl. Mech. Eng. 198 (49) (2009) 3902–3914.
22. D. Benson, Y. Bazilevs, M.-C. Hsu, T. Hughes, A large deformation, rotation-free, isogeometric shell, Comput. Meth. Appl. Mech. Eng. 200 (13) (2011) 1367–1378.
23. D. Millán, A. Rosolen, M. Arroyo, Nonlinear manifold learning for meshfree finite deformation thin-shell analysis, Int. J. Numer. Meth. Eng. 93 (7) (2013) 685–713. doi:10.1002/nme.4403.
24. D. Millán, A. Rosolen, M. Arroyo, Thin shell analysis from scattered points with maximum-entropy approximants, Int. J. Numer. Meth. Eng. 85 (6) (2011) 723–751. doi:10.1002/nme.2992.
25. F. Bassi, S. Rebay, High-order accurate discontinuous finite element solution of the 2D Euler equations, J. Comput. Phys. 138 (2) (1997) 251–285.
26. T. J. Barth, Simplified numerical methods for gas dynamics systems on triangulated domains, Ph.D. thesis, Stanford University (1998).
27. S. Dey, M. S. Shephard, J. E. Flaherty, Geometry representation issues associated with p-version finite element computations, Comput. Meth. Appl. M. 150 (1–4) (1997) 39–55.
28. X. Luo, M. S. Shephard, J.-F. Remacle, The influence of geometric approximation on the accuracy of higher order methods, in: 8th Int. Conf. Numerical Grid Generation in Computational Field Simulations, 2002.
29. D. Xue, L. Demkowicz, Control of geometry induced error in hp finite element (FE) simulations. I. Evaluation of FE error for curvilinear geometries, Int. J. Numer. Anal. Mod. 2 (3) (2005) 283–300.
30. R. Sevilla, S. Fernández-Méndez, A. Huerta, NURBS–Enhanced Finite Element Method (NEFEM): a seamless bridge between CAD and FEM, Arch. Comput. Meth. Eng. 18 (4) (2011) 441–484.
31. S. Dey, R. O'Bara, M. S. Shephard, Curvilinear mesh generation in 3D, Comput. Aided Design 33 (2001) 199–209.
32. X. Luo, M. S. Shephard, J.-F. Remacle, R. O'Bara, M. Beall, B. Szabó, R. Actis, P-version mesh generation issues, in: Proc. 11th Int. Meshing Roundtable, Springer Berlin Heidelberg, 2002, pp. 343–354.
33. X. Luo, M. S. Shephard, R. O'Bara, R. Nastasia, M. Beall, Automatic p-version mesh generation for curved domains, Eng. Comput. 20 (3) (2004) 273–285.
34. M. S. Shephard, J. E. Flaherty, K. Jansen, X. Li, X. Luo, N. Chevaugeon, J.-F. Remacle, M. Beall, R. O'Bara, Adaptive mesh generation for curved domains, Appl. Numer. Math. 52 (2-3) (2005) 251–271.
35. S. Sherwin, J. Peiró, Mesh generation in curvilinear domains using high-order elements, Int. J. Numer. Meth. Eng. 53 (1) (2002) 207–223.
36. P.-O. Persson, J. Peraire, Curved mesh generation and mesh refinement using lagrangian solid mechanics, in: Proc. 47th AIAA, 2009.
37. Z. Xie, R. Sevilla, O. Hassan, K. Morgan, The generation of arbitrary order curved meshes for 3D finite element analysis, Comput. Mech. 51 (2012) 361–374.
38. T. Toulorge, C. Geuzaine, J.-F. Remacle, J. Lambrechts, Robust untangling of curvilinear meshes, J. Comput. Phys. 254 (2013) 8 – 26.
39. A. Gargallo-Peiró, X. Roca, J. Peraire, J. Sarrate, Optimization of a regularized distortion measure to generate curved high-order unstructured tetrahedral meshes, Int. J. Numer. Meth. Eng. 103 (2015) 342–363.
40. A. Mitchell, G. Phillips, E. Wachspress, Forbidden shapes in the finite element method, IMA J. Appl. Math. 8 (2) (1971) 260.
41. D. Field, Algorithms for determining invertible two-and three-dimensional quadratic isoparametric finite element transformations, Int. J. Numer. Meth. Eng. 19 (6) (1983) 789–802.
42. M. Baart, E. Mulder, A note on invertible two-dimensional quadratic finite element transformations, Commun. Appl. Numer. M. 3 (6) (1987) 535–539.
43. A. Johnen, J.-F. Remacle, C. Geuzaine, Geometrical validity of curvilinear finite elements, J. Comput. Phys. 233 (2013) 359 – 372.
44. A. Salem, S. Canann, S. Saigal, Robust distortion metric for quadratic triangular 2D finite elements, Appl. Mech. Div. ASME. 220 (1997) 73–80.
45. A. Salem, S. Canann, S. Saigal, Mid-node admissible spaces for quadratic triangular arbitrarily curved 2D finite elements, Int. J. Numer. Meth. Eng. 50 (2) (2001) 253–272.
46. K. Yuan, Y. Huang, T. Pian, Inverse mapping and distortion measures for quadrilaterals with curved boundaries, Int. J. Numer. Meth. Eng. 37 (5) (1994) 861–875.
47. P. M. Knupp, Label-invariant mesh quality metrics, in: Proc. 18th Int. Meshing Roundtable, Springer Berlin Heidelberg, Salt Lake City, 2009, pp. 139–155.
48. L. Branets, G. Carey, Extension of a mesh quality metric for elements with a curved boundary edge or surface, J. Comput. Inf. Sci. Eng. 5 (4) (2005) 302–308.

49. A. Salem, S. Saigal, S. Canann, Mid-node admissible space for 3D quadratic tetrahedral finite elements, Eng. Comput. 17 (1) (2001) 39–54.
50. P. L. George, H. Borouchaki, Construction of tetrahedral meshes of degree two, Int. J. Numer. Meth. Eng. 90 (9) (2012) 1156–1182.
51. X. Roca, A. Gargallo-Peiró, J. Sarrate, Defining quality measures for high-order planar triangles and curved mesh generation, in: Proc. 20th Int. Meshing Roundtable, Springer International Publishing, 2012, pp. 365–383.
52. A. Gargallo-Peiró, X. Roca, J. Peraire, J. Sarrate, Defining quality measures for mesh optimization on parameterized CAD surfaces, in: Proc. 21st Int. Meshing Roundtable, Springer International Publishing, 2013, pp. 85–102.
53. A. Gargallo-Peiró, X. Roca, J. Peraire, J. Sarrate, Defining quality measures for validation and generation of high-order tetrahedral meshes, in: Proc. 22nd Int. Meshing Roundtable, Springer International Publishing, 2014, pp. 109–126.
54. P. M. Knupp, Algebraic mesh quality metrics, SIAM J. Numer. Anal. 23 (1) (2001) 193–218.
55. P. M. Knupp, Algebraic mesh quality metrics for unstructured initial meshes, Finite Elem. Anal. Des. 39 (3) (2003) 217–241.
56. A. Gargallo-Peiró, X. Roca, J. Sarrate, A surface mesh smoothing and untangling method independent of the CAD parameterization, Comput. Mech. 53 (4) (2014) 587–609. doi:10.1007/s00466-013-0920-1.
57. S. Dey, R. O'Bara, M. S. Shephard, Towards curvilinear meshing in 3D: the case of quadratic simplices, Comput. Aided Design 33 (3) (2001) 199–209.
58. X. Luo, An automatic adaptive directional variable p-version method in 3d curved domains, Ph.D. thesis, Rensselaer Polytechnic Institute (2005).
59. X. Jiao, D. Wang, Reconstructing high-order surfaces for meshing, Eng. Comput. 28 (4) (2012) 361–373.
60. B. Clark, N. Ray, X. Jiao, Surface mesh optimization, adaption, and untangling with high-order accuracy, in: X. Jiao, J.-C. Weill (Eds.), Proc. 21st Int. Meshing Roundtable, Springer Berlin Heidelberg, 2013, pp. 385–402.
61. J.-F. Remacle, T. Toulorge, J. Lambrechts, Robust untangling of curvilinear meshes, in: Proc. 21st Int. Meshing Roundtable, Springer International Publishing, 2013, pp. 71–83.
62. S. Sastry, S. Shontz, S. Vavasis, A log-barrier method for mesh quality improvement, in: Proc. 20th Int. Meshing Roundtable, Springer International Publishing, 2012, pp. 329–346.
63. J. M. Escobar, E. Rodríguez, R. Montenegro, G. Montero, J. M. González-Yuste, Simultaneous untangling and smoothing of tetrahedral meshes, Comput. Meth. Appl. Mech. Eng. 192 (25) (2003) 2775–2787.
64. O. CASCADE, Open CASCADE Technology, 3D modeling and numerical simulation, `www.opencascade.org` (2012).
65. X. Roca, J. Sarrate, A. Huerta, Surface mesh projection for hexahedral mesh generation by sweeping, in: Proc. 13th Int. Meshing Roundtable, Springer Berlin Heidelberg, 2004, pp. 169–179.
66. X. Roca, J. Sarrate, A. Huerta, Mesh projection between parametric surfaces, Commun. Numer. Met. Eng. 22 (6) (2006) 591–603.
67. X. Roca, Paving the path towards automatic hexahedral mesh generation, Ph.D. thesis, Universitat Politècnica de Catalunya (2009).
68. T. Warburton, An explicit construction of interpolation nodes on the simplex, J. Eng. Math. 56 (3) (2006) 247–262.
69. A. Gargallo-Peiró, Validation and generation of curved meshes for high-order unstructured methods, Ph.D. thesis, Universitat Politècnica de Catalunya (2014).
70. J. Nocedal, S. Wright, Numerical optimization, Springer Verlag, 1999.